Tampere University

Paula Kölhi

COMPARISON OF DOSIMETRIC QUALITY ASSURANCE METHODS FOR STEREOTACTIC TREATMENT PLANS

Faculty of Medicine and Health Technology
Licentiate thesis
October, 2019

ABSTRACT

Paula Kölhi: Comparison of dosimetric quality assurance methods for stereotactic treatment plans
Licentiate Thesis
Tampere University
Doctoral programme in Biomedical Sciences and Engineering
October 2019

Radiation therapy is an important cancer treatment method. Radiation therapy techniques have advanced rapidly during last decades. Implementation of intensity modulated treatments with modern image guidance has enabled conformal dose distributions and high geometrical accuracy. Stereotactic radiation therapies are high precision treatments with high radiation doses for small targets. The accuracy requirements are highlighted in stereotactic treatments and quality assurance of treatment plans is an important procedure.

The aim of this thesis was to quantitatively compare the performance of different commercial quality assurance systems for quality assurance (QA) of stereotactic treatment plans with volumetric modulated arc therapy technique using flattening filter free (FFF) beams (6 MV FFF or 10 MV FFF). 48 clinical treatment plans (20 brain, 19 lung and 9 prostate tumors) were verified using a portal dosimetry system and a 2D array detector. The portal dosimetry measurements were acquired with Varian aS1200 electronic portal imaging device. The 2D array detector was IBA I'mRT MatriXX Evolution. Gamma index analysis was performed with gamma criteria of 3% dose difference and 3 mm distance to agreement (3%/3 mm), 2%/2 mm, 1%/1 mm and 3%/1 mm. Average percentual dose difference was also evaluated from portal dosimetry measurements. Energy dependency was investigated comparing results from treatment plans with 6 MV FFF and 10 MV FFF beams. Effect of analysis threshold was examined with threshold values of 5% and 60% from the maximum dose. Portal dosimetry for treatment plans with 6 MV FFF beams was carried out with two different portal dose prediction algorithms (Varian Portal Dose Image Prediction PDIP and Anisotropic Analytical Algorithm AAA).

The results show that as the target volume increases, the gamma passing rates increase in portal dosimetry measurements for brain and lung tumors. I'mRT MatriXX Evolution measurement results show significant target volume dependency, gamma passing rates increasing as the volume increases in all the target site groups.

PDIP and I'mRT Matrixx Evolution measurement results show energy dependency (6 MV FFF vs. 10 MV FFF). PDIP measurements result in higher gamma passing rates for treatment plans with 6 MV FFF than 10 MV FFF. I'mRT MatriXX Evolution measurements result in higher gamma passing rates with 10 MV FFF than 6 MV FFF. The analysis threshold value affects the results in varying amount depending on the measurement setup, indicating the importance of preselected threshold in QA protocols.

Portal dosimetry measurements with PDIP-algorithm result in higher gamma passing rates than measurements with AAA-algorithm. Comparison of portal dosimetry with both algorithm and array detector measurements with I'mRT MatriXX Evolution show that the measurement method has a significant effect on measurement results. The gamma passing rates decrease and the deviations increase from PDIP to AAA and AAA to I'mRT MatriXX Evolution. PDIP results correlate with AAA results, but I'mRT MatriXX Evolution results do not correlate with portal dosimetry results.

In conclusion, the QA results of stereotactic treatment plans are dependent on the measurement system, beam energy, target volume and analysis parameters. The QA results obtained with different measurement systems cannot be compared directly. This thesis gives quantitative information for Varian portal dosimetry and IBA I'mRT MatriXX Evolution -array detector.

Keywords: portal dosimetry, quality assurance of treatment plans, pretreatment verification, stereotactic body radiotherapy, stereotactic radiosurgery, EPID, aS1200, I'mRT MatriXX Evolution, PDIP, AAA, FFF, VMAT

TIIVISTELMÄ

Paula Kölhi: Stereotaktisten potilassuunnitelmien dosimetristen laadunvarmistus-menetelmien vertailu
Lisensiaatin tutkimus
Tampereen yliopisto
Biolääketieteen tekniikan tohtoriohjelma
Lokakuu 2019

Sädehoito on tärkeä syövän hoitomuoto. Sädehoitotekniikat ovat kehittyneet nopeasti viimeisten vuosikymmenien aikana. Intensiteetti muokatun sädehoidon käyttöönotto yhdessä nykyaikaisten kuvantaohjaustekniikoiden kanssa ovat mahdollistaneet konformaaliset annosjakaumat sekä korkean geometrisen tarkkuuden. Stereotaktiset sädehoidot ovat korkean tarkkuuden hoitoja suurilla sädeannoksilla pieniin kohteisiin. Tarkkuusvaatimukset korostuvat stereotaktisissa hoidoissa ja potilassuunnitelmien laadunvarmistus on tärkeä työvaihe.

Tämän tutkimuksen tarkoitus oli verrata kvantitatiivisesti eri kaupallisten mittalaitteiden suorituskykyä stereotaktisten potilassuunnitelmien laadunvarmistuksessa. Potilassuunnitelmat on toteutettu kaarihoitotekniikalla hyödyntäen tasoittamattomia säteilykeiloja (6 MV FFF ja 10MV FFF). 48 kliinistä potilassuunnitelmaa (20 aivokasvainta, 19 keuhkokasvainta ja 9 eturauhasen kasvainta) verifioitiin käyttämällä portaalidosimetriaa sekä 2D tasoilmaisinta. Portaalidosimetria toteutettiin Varianin aS1200-ilmaisimella ja tasoilmaisimena käytettiin IBA:n I'mRT MatriXX Evolution –tasoilmaisinta. Gamma indeksi analyysi toteutettiin gamma kriteereillä 3% annosero ja 3 mm etäisyys ero (3%/3 mm), 2%/2 mm, 1%/1 mm and 3%/1 mm. Portaalidosimetriatuloksista määritettiin myös keskimääräinen prosentuaalinen annosero. Energian vaikutusta tutkittiin vertaamalla tuloksia suunnitelmista jotka on toteutettu energioilla 6 MV FFF tai 10 MV FFF. Analyysikynnyksen vaikutusta tutkittiin vertaamalla kahdella eri kynnyksellä (5% ja 60%) saatuja tuloksia. 6 MV FFF-energialla toteutetut potilassuunnitelmat lasketettiin kahdella eri portaalidosimetria algoritmilla, Varianin Portal Dose Image Prediction (PDIP)-algoritmilla, sekä Anisotropic Analytical (AAA)-algoritmilla.

Portaalidosimetriatulokset osoittavat, että kohteen kasvaessa, gamma-analyysin hyväksymisprosentit kasvavat aivo- ja keuhkokasvainten osalta. I'mRT MatiXX Evolution –ilmaisimella gamma-analyysin hyväksymisprosentit kasvavat ja hajonta pienenee kaikkien kasvainryhmien välillä kun kohteen koko kasvaa.

Energiariippuvuus osoitettiin sekä PDIP-portaalidosimetrialla, että I'mRT Matrixx Evolution –mittauksissa. Portaalidosimetrialla gamma-analyysin hyväksymisprosentit huononevat kun käytetään 10 MV FFF-energiaa, verrattuna 6MV FFF-energiaan. I'mRT MatriXX Evolution –tasoilmaisimella hyväksymisprosentit kasvavat kun käytetään 10 MV FFF-energiaa. Analyysikynnys vaikuttaa tuloksiin vaihtelevalla tavalla riippuen mittausasetelmasta, osoittaen etukäteen valitun analyysikynnyksen tärkeyttä laadunvarmistusprotokollassa.

Portaalidosimetria PDIP-algoritmilla antaa korkeampia hyväksymisprosentteja kuin AAA-algoritmilla. Kun portaalidosimetriaa verrataan tasoilmaisimeen, havaitaan että mittausmenetelmä vaikuttaa tuloksiin merkitsevästi. AAA-algoritmilla saadut hyväksymisprosentit ovat huonompia kuin PDIP-algoritmilla saadut ja tasoilmaisimella saadut hyväksymisprosentit ovat edelleen huonompia ja hajonta suurempaa kuin AAA-algoritmilla. Portaalidosimetriatulokset eri algoritmeilla korreloivat keskenään, mutta tasoilmaisimella saadut tulokset eivät korreloi portaalidosimetriatulosten kanssa.

Yhteenvetona voidaan todeta, että stereotaktisten potilassuunnitelmien laadunvalvontatulokset riippuvat mittaussysteemistä, käytetystä energiasta, kohteen koosta sekä analyysiparametreista. Eri mittalaitteilla saatuja mittaustuloksia ei voida suoraan verrata toisiinsa. Tämä työ antaa kvantitatiivista informaatiota Varianin portaalidosimetriasta sekä IBAn I'mRT Matrixx EVolution –tasoilmaisimesta.

Avainsanat: portaalidosimetria, potilassuunnitelmien laadunvarmistus, stereotaktinen sädehoito, aS1200, I'mRT MatriXX Evolution, PDIP, AAA, FFF, VMAT

PREFACE

This licentiate thesis was carried out in Department of Radiotherapy in Tampere University Hospital. I wish to express my gratitude for my supervisor professor Hannu Eskola and my instructors in this thesis, Chief physicist Mika Kapanen and physicist Antti Vanhanen for their guidance in my research. I also appreciate all the help and advice I got from all the physicists in the Department of Radiotherapy.

Tampere, October 6, 2019

Paula Kölhi

TABLE OF CONTENTS

ABBREVIATIONS

10 FFF	10 MV flattening filter free energy
10X	10 MV flattened beam energy
6 FFF	6 MV flattening filter free energy
6X	6 MV flattened beam energy
AAA	Anisotropic Analytical Algorithm
ACROP	Committee in ESTRO
aS1200	Varian portal detector
aSI	Amorphous-silicon
BED	Biologically effective dose
CA	Collimator angle
CTV	Clinical target volume
CU	Calibrated unit
DLG	Dosimetric leaf gap
dMLC	Dynamic MLC
DTA	Distance-to-agreement
EPID	Electronic portal imaging device
ESTRO	The European Society for Radiotherapy and Oncology
FF	Flattened beam
FFF	Flattening filter free
GA	Gantry angle
HDMLC	High definition multileaf collimator
IMRT	Intensity modulated radiation therapy
linac	Linear accelerator
LMC	Leaf motion calculator
LPO	Leaf position offset
Max	Maximum value
Min	Minimum value
MLC	Multileaf collimator
MU	Monitor unit
PDIP	Portal Dose Image Prediction algorithm
PO	Photon Optimization Algorithm
PRO	Progressive Resolution Optimizer algorithm
PTV	Planning target volume
QA	Quality assurance
RFO	Radiation field offset
ROI	Region of interest
SAD	Source to axis distance
SBRT	Stereotactic body radiation therapy
SD	Standard deviation
SDD	Source to detector distance
SID	Source to imager distance
SRS	Stereotactic radiosurgery
SSD	Source to surface distance
TAUH	Tampere University Hospital
VMAT	Volumetric modulated arc therapy

1. INTRODUCTION

Radiation therapy is an important treatment method in cancer treatments. Radiation therapy techniques have advanced rapidly during last decades. Implementation of intensity modulated treatments with modern image guidance has enabled high geometrical accuracy and conformal dose distribution in the target while sparing the surrounding tissues from high radiation doses. (1) Stereotactic radiation therapy treatments are characterized by small target volumes treated into high biologically effective doses by a single dose or a few fractionated doses. Steep dose gradient in stereotactic treatments, together with the small target size and high radiation dose, set high requirements for geometrical accuracy and quality assurance (QA) of the treatment plans. (2) The use of flattening filter free (FFF) beams enable the use of high dose rates resulting in the reduction of treatment times. The importance of reduced treatment time in stereotactic treatments is highlighted, due to the high fraction doses and uncomfortable patient immobilization often required for stereotactic treatments.

In daily practice of treatment plan QA, the effortlessness and speed of QA procedures are important factors. Sufficient spatial resolution and online measurements are required. Electronic portal imaging devices (EPID) and array detectors are easy to use measurement devices capable of online measurements. The QA of treatment plans is based on the comparison of measured and predicted dose distributions. (3) The dose distribution analysis is commonly performed with gamma index method (4). The use of gamma index method requires determination of analysis parameters used: dose deviation, distance-to-agreement, pixels to be analyzed and gamma pass rate criterion. Varian (Varian Medical Systems, Palo Alto, CA) offers an EPID capable of measuring FFF-beams with high dose rate without saturation and two different algorithms (Portal Dose Image Prediction (PDIP) and Anisotropic Analytical Algorithm (AAA)) for portal dose calculation for 6 MV FFF (6 FFF) beams. (5)

The aim of this thesis was to determine the current status of QA of stereotactic treatment plans with FFF-beams and to investigate the performance of Varian aS1200-EPID and I'mRT MatriXX Evolution (IBA Dosimetry GmbH, Schrwarzenbruck, Germany) –array detector in stereotactic treatment plans with FFF-beams. Only a few scientific publications (6, 7) presenting comparisons of QA measurement devices for stereotactic treat-

ment plans with FFF-beams were found in the literature. Scientific publications comparing portal dosimetry with Varian aS1200-EPID and I'mRT MatriXX Evolution array detector were not found. Scientific publications presenting comparisons of PDIP and AAA –algorithms in portal dosimetry were not found.

This thesis consists of two parts: a review of the literature and the practical part of the study. The review of the literature covers the principles of radiation therapy in brief and the dosimetric QA of treatment plans in more detail. The practical part of the study consists of a dosimetric performance study comparing the measurement results applied by Varian portal dosimetry with aS1200-EPID to measurement results applied by I'mRT MatriXX Evolution –array detector.

48 clinical stereotactic treatment plans from three different target sites (20 brain, 19 lung and 9 prostate) previously treated in Tampere University Hospital (TAUH) were included in this retrospective study. The treatment plans comprise a comprehensive set of typical clinical cases. The treatment plans were planned according to the clinical protocols of stereotactic treatments, carried out with volumetric modulated arc therapy (VMAT) technique applying FFF-beams (6 MV FFF or 10 MV FFF). All the treatment plans were measured with both measurement systems and portal dosimetry measurements were performed with both portal prediction algorithms (PDIP and AAA) for treatment plans with 6 MV FFF –beams. The gamma index analysis was performed after the measurements.

This thesis is divided into seven chapters. Chapter 1. presents an introduction and the aim of this thesis. Chapter 2. introduces the theoretical background of the study, presenting the basics of the radiation therapy and dose calculation. Chapter 3. presents the dosimetric QA of treatment plans in more detail. Chapter 4. presents the materials and methods of the study. The results are presented in chapter 5. Chapter 6. discusses the results and chapter 7. concludes this thesis.

2. RADIATION THERAPY AND DOSE CALCULATION

Radiation therapy is a cancer treatment method. Radiation therapy utilizes ionizing radiation to destroy tumor cells. External radiation therapy is given using linear accelerators, which produce photon and electron radiation. In this thesis, we concentrate on external photon beam treatments of small targets with high radiation doses.

The ionizing radiation destroys cells. The higher the total radiation dose, the higher is the amount of destroyed cells, both tumor cells and healthy cells. The survival curves describe the relationship of the cell survival and the radiation dose. (8)

The radiation therapy is fractioned into several smaller fractions to spare normal tissue by repair of sublethal damages and repopulation. Fractionation also increases the tumor cell death by reoxygenation and redistribution. Fractionation schemes were developed experimentally. For relatively small tumors, high precision treatments with few high dose fractions have been developed. (8)

2.1 Linear accelerator

A linear accelerator (linac) is a device that utilizes high frequency electromagnetic waves to accelerate charged particles such as electrons to high energies in a linear tube. Electron beam can be utilized itself to treat superficial tumors near the skin surface. More common case is that the electron beam is bombarded to a high density target and photons are produced as Bremsstrahlung radiation. Photons penetrate much deeper in the tissue than the electrons. (9)

The gantry of the linear accelerator can rotate 360° in the horizontal axis. The collimator rotates in the vertical axis. The isocenter is the point where the collimator axis and the rotation axis intercept. In isocentric treatment technique, the beams from different directions meet in the same point. (9)

A schematic diagram of linear accelerator head is presented in figure 1. After the target, the photons travel through the primary collimators. After the primary collimators, flattening filters located in the carousel, can be set in the photon beam to flatten it. (9)

An ionization chamber is located after the carousel to detect symmetry and dose rate of the beams. After the ionization chamber, the beam is restricted by secondary collimators. The beam can be shaped statically or dynamically by multileaf collimator (MLC) which is

located the outmost in the treatment head. The leaves of the MLC move appropriately during the radiation treatment. (9)

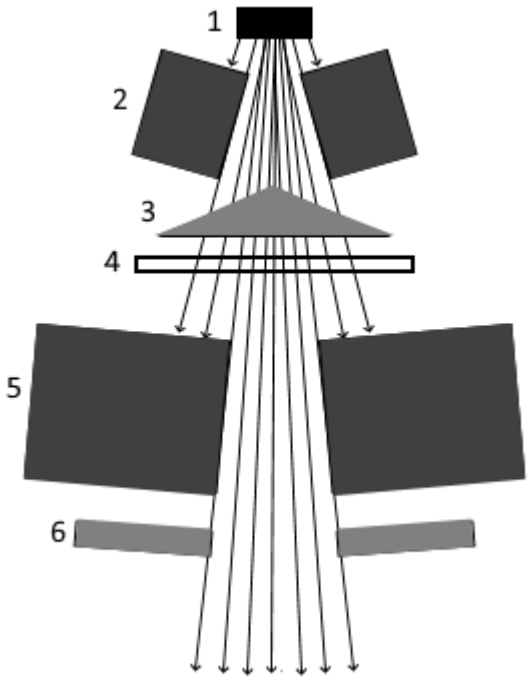

Figure 1. *Schematic diagram of linear accelerator head. 1) Target 2) Primary collimators 3) Flattening filter 4) Ionization chamber 5) Jaws 6) MLC*

2.1.1 Multileaf collimator

Varian TrueBeam STx linac, used in this study, is equipped with high definition MLC (HDMLC) with 120 leaves. In Varian MLC, the ends of the leaves are rounded in order to ensure relatively constant penumbra at different positions in the field. The HDMLC leaves have a curvature of 16 cm. A schematic illustration of HD120™ MLC leaf tip shape is presented in figure 2. (10)

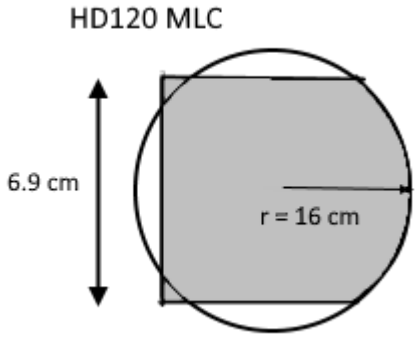

Figure 2. *Schematic illustration of leaf tip shape of Varian HD120 MLC*

The leakage between adjacent leaves is minimized by the tongue and groove arrangement. The motion of the leaves is rectilinear. The rectilinear motion and rounded leaf ends in combination introduce a nonlinear dependence of field size on leaf position. In dynamic MLC treatments, the delivered photon fluence is sensitive to the transmission through the leaves and the rounded leaf ends as well as the leakage between the leaves and the head scatter. (10)

2.1.2 Flattening filter free photon beams

In conventional linacs, the photon distribution produced in the target is peaked: the intensity of the radiation field is higher in the central axis of the radiation field. Flattening filters are utilized to create flattened beams [6MV FFF (6 FFF), 10 MV FFF (10 FFF)], but a large proportion of the beam intensity is removed by the flattening filters reducing the highest possible dose rate. The majority of this intensity is converted into scattered radiation. The conventional radiation therapy techniques required flattened fields, but with intensity modulated techniques, a non-uniform beam profile can be taken into account in the treatment planning system during the inverse optimization. The advantages of the FFF beams are shorter treatment times due to the higher dose rates and reduction of the out-of-field dose due to the absence of scatter and leakage from the flattening filter. A schematic illustration of flattened and unflattened beam profiles are presented in figure 3. (6, 11, 12)

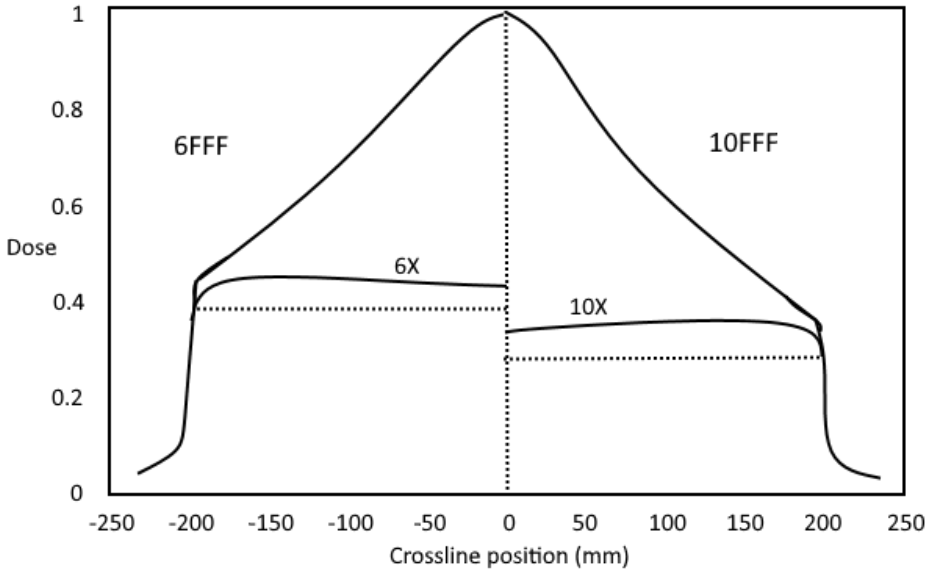

Figure 3. *Schematic illustration of flattened (6X and 10X) and unflattened (6FFF and 10FFF) beam profiles.*

2.2 Intensity modulated radiation therapy

Intensity modulated radiation therapy (IMRT) is a treatment technique in which the intensity of the beam in different parts of the radiation field is modified. IMRT enables precise conformation of the radiation dose to the target volume allowing more normal tissue to be spared than with other techniques. On the other perspective, the tumor dose can be increased with IMRT, compared to the conventional techniques, without increasing the dose in the surrounding critical tissues. However, small doses cover larger regions in the body compared to the traditional planning techniques. (9, 13)

IMRT has two key features compared to the conventional radiotherapy: non-uniform intensity of the radiation beams and inverse planning. The inverse planning is a planning method in which the desired dose distribution in the means of clinical objectives are set at first, and then the treatment parameters are determined by optimization to achieve the desired dose distribution. Optimization criteria have to be described in a quantitative form, normally as dose limitations for target and critical structures. The optimal dose distribution is calculated using an iterative mathematical method. As a result, the dose distribution fulfils given criteria in an optimal way, depending on the mathematical method and the optimization criteria. If optimization criteria are opposing each other, the optimization needs to make a compromise. The result is also affected by the starting point of the optimization, which is characterized usually by the selection of the radiation type and energy, the number of fields, treatment technique, field angles, collimator angles and field sizes. The starting point definition makes calculations faster by restricting the options. At the same time, it also restricts the degrees of freedom in optimization and the most optimal dose plan. The starting point definition might need revision, if the dose plan does not meet the given criteria. (9, 13)

VMAT is an IMRT technique in which the dose is delivered dynamically during the rotation of the gantry: 360 degrees of beam directions are available for optimization. VMAT utilizes also dynamic MLCs and dose rate. MLC leaf motion and number of monitor units (MU) per degree of gantry rotation are restricted during the optimization. (14)

2.2.1 Modulation

IMRT/VMAT technique enables conformal dose distributions in targets and sparing of normal tissues by concave shaped distributions. The most optimal dose distribution is a trade of complexity of the treatment plan and the desired dose distribution. As the complexity increases, also the degree of modulation increases and the accuracy of the plan delivery might decrease. An optimal treatment plan has good enough dose distribution with as low degree of complexity as practically possible. As the modulation of the beam

increases, a large number of small and irregular beam apertures are used. The number of MUs increases as the MLC blocks the beam for increasing amount and the radiation energy is lost in the primary beam and the secondary radiation is increased due to the scatter and transmission through the MLC leaves. The increase of modulation degree increases also the dose calculation uncertainties, as well as MLC movement, gantry movement and dose rate uncertainties. As a result, the increase of modulation degree increases the probability of dose delivery errors and the intended dose distribution might not be delivered accurately to the patient. (15)

2.3 Dose calculation

A clinical beam is represented by a photon beam source model in Varian Eclipse treatment planning system. The photon beam source model consists of four main sources: primary photon source, second photon source, electron contamination source and wedge scatter source. (16)

The primary source of the photon beam source model is a point source located at the target plane. The primary source models the bremsstrahlung photons created in the target, but does not take into account the photons that interact with the treatment unit head. The second source is a Gaussian plane source. It is located at the bottom of the flattening filter. It models the photons that result from interactions in the treatment unit head. In case of FFF-beams, the second source is not taken into the calculations, as the flattening filter is removed from the beamline and since the most important source of scattering is not present. (16)

Electron contamination describes the dose deposited in the build-up region that the primary and the second source models do not take into account. It also models the photon contamination due to the electron interactions. The electron contamination model is a depth-dependent curve and it describes the total amount of electron contamination dose at a certain depth. In the wedge scatter source, each point in the wedge acts as a scatter source. The intensity of the scattered radiation is proportional to the amount of primary radiation hitting that point. (16)

The dose calculation algorithm used routinely in our clinic is the algorithm originally conceived by Dr. Ulmer and Dr. Kaissl (17), the Anisotropic Analytical Algorithm (AAA), which is a 3D pencil beam convolution/superposition algorithm. It uses separate Monte Carlo derived modeling for each source component. The AAA accounts for tissue heterogeneity anisotropically by using photon scatter kernels in multiple lateral directions. (16)

The patient scatter model is used for the dose deposited inside the patient and the phase-space parameters describe the treatment beam upstream of the patient. The broad treatment beam is divided into finite-sized beamlets. The beamlets are modelled using several monoenergetic scatter kernels, which describe the phantom-scatter. The size of the beamlets is determined by the resolution of the calculation grid on the isocenter plane. The dose calculation is based on the convolutions over the beamlet cross-sections separately for each source model component. (16)

The patient body volume is divided into a matrix of 3D voxels to calculate the volumetric dose distribution. The geometry of the calculation voxel grid is divergent due to the divergent beam fanlines. Calculation voxels are associated with the mean electron density that is computed from the patient computed tomography (CT) images according to a user-specified calibration curve. The 3D dose distribution is calculated from separate convolutions for different sources in the source model. The convolutions are performed for the broad treatment beam which comprises all finite-sized beamlets. The final dose is obtained by a simple superposition of the individual beamlet contributions. (16)

The photon beam attenuation is modelled with an energy deposition density function and the photon scatter is modelled with a scatter kernel that defines the lateral energy scattering. The photon beam attenuation and the scatter kernel are defined individually for each beamlet. The calculations of the primary source and the other photon sources differ only by the spectral composition and the position and size of the focal spots. The dose convolution is performed in terms of energy, which allows more accurate energy conservation even in complex heterogeneous convolutions. Finally the scaled-water approximation is used to convert the energy to dose. (16)

2.3.1 VMAT calculation

In Varian Eclipse treatment planning system, the optimization of IMRT/VMAT plans can be done by Photon Optimization Algorithm (PO) or Progressive Resolution Optimizer (PRO) algorithm. The PO algorithm combines the previous Varian optimization methods used for static field IMRT and arc field IMRT with Dose Volume Optimizer- and PRO-algorithms. The main difference of the PO algorithm from the PRO algorithm is that the PRO-algorithm uses a point cloud model for defining structures. The PO algorithm uses a structure model for defining structures, where structures, dose volume histogram calculation and dose sampling are defined spatially by using one single matrix over the image. (16)

The optimization algorithms PO and PRO create VMAT plans, which use dynamic MLC (dMLC), variable dose rate and variable gantry speed, based on dose-volume objectives.

A sequence of control points is generated to define MLC leaf positions and MUs per degree as a function of gantry angle. MUs per degree are encoded with the cumulative meterset weight, defining the increase in monitor units between control points relative to the total MUs in the field. This information is transferred to the treatment machine and the machine control system determines how dose rate and gantry speed will be modulated to deliver the plan. (16)

An objective function, the sum of the dose-volume and other user-defined objectives, is used to optimize the plan and to evaluate its quality. The PO and PRO algorithms use a progressive resolution principle. The initial conditions are defined using control points to represent each VMAT field. At first, the dose is modelled using a lower number of dose calculation segments evenly distributed in each field. The number of segment increases from one multi-resolution level to the next. The dose in each segment is calculated from the combined fluence through the MLC aperture at the control points located within a certain sector of the arc. Leaf motion is modelled by interpolating leaf positions between the control points. Leaf tongues are taken into account by modifying the MLC aperture outline to effectively account for the tongue-and-groove effect. The number of control points remains the same during the whole optimization, but the angle resolution of the dose calculation segments gets more accurate as the optimization progresses leading to the more accurate dose calculation. The optimization algorithms give their results as fluences. (16)

In Eclipse, the final dose calculation for all MLC fields is based on fluences. All fluence delivery modelling algorithms take into account the leaf transmission, dosimetric leaf gap and tongue-and-groove modelling. These features are also taken into account in the PO and PRO algorithms, as well as in the final fluence calculation for MLC fields. (16)

A leaf motion calculator (LMC) program calculates the dMLC leaf motion pattern to deliver the dose defined by the optimal fluence. Taking into account the physical and mechanical characteristics of the MLC device, the resulting fluence is an actual fluence that approximates the optimal fluence. (16)

Four parameters are required in the commissioning of the Varian MLC: leaf position offset (LPO), radiation field offset (RFO), dosimetric leaf gap (DLG) and the MLC transmission.

There are three possible projections of the rounded leaf ends at the isocenter, the geometric position, the physical position and the projected position. The geometric position is defined by the light field. The physical position is defined by the radiation field edge defined as the 50% isodose line. The projected position is defined by Varian in a MLC

file which links the projected position with the light field (LPO), as the projected position has a nonlinear dependency with the light position. RFO is defined as the difference between the geometric position and the physical position. The Varian Eclipse defines the nominal position of the MLC in the light field. The algorithm decreases the MLC position values by the constant RFO parameter in order to align the nominal MLC position with the modelled radiation field. (18)

DLG

DLG is a parameter which takes into account the partial transmission through rounded leaf ends of the MLC. The MLC is modelled as straight edged in the Eclipse treatment planning system, and the dose calculation in Eclipse retracts the MLC leaf positions by half of the DLG for all leaf positions in a dMLC plan to model the rounded leaf ends. As each leaf tip is retracted by half of the DLG, the gap between the fully closed leaf pair equals the DLG. (16, 19)

The DLG models the difference between the radiation and light field accounting for inherent leakage between leaf tips. The DLG in the treatment planning system is determined during commissioning of the linac and is set individually for each energy in the linear accelerator. It can be measured by extrapolating the size of static or dynamic fields formed by MLC leaves to the size under which the measured dose equals the MLC leakage. Due to the uncertainties, the use of measured DLG in a dose calculation algorithm often results with lower agreement than expected between the planned and the measured dose. The higher failure rates are reported with very large or very small target volumes surrounded by sensitive organs. Large number of monitor units are required in a single fraction high dose treatments and the accuracy of leakage calculations becomes a critical issue as it accounts for much of the patient dose. (18-21)

The DLG can be measured with a series of dMLC setups (10). The dose of the sweeping gap dMLC motion with various gap widths is measured. The measured leaf transmission is subtracted from the sweeping gap measurements. The corrected sweeping gap measurements are plotted against nominal gap width and regression is fitted to the measurement points. DLG can be obtained by extrapolating the regression line to zero measurement and reading the corresponding gap width. The extrapolated gap width should be negative and DLG is the absolute value of it. (16)

MLC transmission

The MLC leaves do not block the radiation completely. Small amount of radiation transmits directly through the leaves. The transmission factor is a ratio of the measured dose in an open field of certain field size and the measured dose with the same field size, but

all the MLC leaves closed behind the jaws. The leaf transmission factor describes the average transmission through the MLC leaves, but does not take into account the local variations in leaf width or in the energy spectrum of the beam. (16)

In the leaf travel direction, the path length of the beam through the MLC leaves increases as the off-axis distance increases. This decreases the intraleaf transmission at off-axis distances along the MLC travel direction. In the direction perpendicular to MLC motion, the leaves are arranged to follow the divergence of the beam and thus the path lengths are equal. Despite the equal path lengths, the intraleaf transmission through the central 40 MLC leaf pairs (width 0.5cm) is greater than the outer leaf pairs (width 1.0cm). (19)

Tongue-and-groove

To minimize the inter-leaf leakage, the Varian MLC device models have a tongue-and-groove design. The tongue of the MLC blocks some of the additional radiation and the amount is proportional to the ratio between the tongue and the leaf widths. This is called the tongue-and-groove effect. This effect is modelled in the fluence delivery algorithms by extending the leaf projections in the direction perpendicular to the leaf motion with an approximate extension parameter, which is slightly smaller than the real tongue width. (16)

2.4 Stereotactic radiation therapy

Originally high precision radiation therapy treatments were given using external coordinates and the treatment was called stereotactic radiation therapy. Originally stereotactic radiosurgery (SRS) treatments were given solely on small targets in the brain. Stereotactic frame was screwed on a surface of the scull bone (before treatment planning computed tomography imaging) for a single fraction treatments. For treatments with several fractions, the stereotactic frame was attached on a mask system made of thermoplastic material. (13)

Later on stereotactic body radiation therapy (SBRT) with a stereotactic body frame and finally frameless stereotactic treatments were developed. In frameless stereotactic treatments, the external coordinates are set based on the markers on the patient skin, instead of the external frame. Nowadays all the high precision treatments are based on the frameless stereotaxy and no frames are used any more. However, the term “stereotactic treatment” is still in use, although the high precision treatments are not based on external coordinates any more. To assure accurate tumor localization, proper patient immobilization, motion limitation and modern image guidance are needed.(13)

Stereotactic treatments are characterized by the small target volumes treated by a single high dose or few fractionated doses. Fractionated stereotactic treatments are usually given in a few (2-3) fractions a week, instead of the 5 fractions a week (conventional treatments). The number of fractions is low (1-5 fractions) compared to the conventional treatments (20-30 fractions). The aim of the stereotactic treatments is to get a steep dose gradient between the target and the organs next to the target, in order to minimize the volume of the healthy tissue that is affected by the high radiation dose. (2)

SRS for brain has showed the clinical usefullness in the treatment of brain tumors. SBRT is highly effective in early stage primary and oligometastatic cancers in abdominopelvic and thoracic areas, as well as at spinal and paraspinal locations. The stereotactic treatments result in a high biological effective dose (BED) and require high level of accuracy in the entire treatment delivery process. In general, larger number of beams are needed, as well as non-coplanar beam arrangements, compared to the conventional treatments. (22)

Nowadays, the use of VMAT treatment technique in stereotactic high-precision treatments is increasing. ESTRO ACROP Guideline of SBRT for peripherally located early stage non-small cell lung cancer recommends VMAT for best practice (23). In VMAT treatments, multiple arcs are required to deliver large fraction doses and FFF-beams are utilized to minimize the treatment time.

3. DOSIMETRIC QUALITY ASSURANCE OF TREATMENT PLANS

3.1 Small field dosimetry

Advanced radiation therapy techniques with increased tumor dose and decreased dose at organs at risk in means of steep dose gradients have increased the accuracy requirements for dose delivery to patients. The QA of treatment plans is one important step to guarantee the accuracy requirements. (24)

For conventional radiation therapy, dosimetry protocols are based on well-established practices based on measurements using an ionization chamber. The ionization chamber measurements require calibration coefficient in terms of absorbed dose to water, which is traceable to a primary standards dosimetry laboratory for reference conditions. Nowadays, the advances in radiotherapy treatments has led to the use of small fields of a subcentimeter scale in radiation therapy, compared to the traditional radiation therapy fields from 4 x 4 cm^2 to the 40 x 40cm^2. The dramatic increase in the amount of small fields utilized in radiotherapy treatments is due to the use of MLC collimated beamlet-based IMRT and VMAT treatment techniques, especially in stereotactic treatments. The dosimetric accuracy previously achieved for standard treatments is at risk for both absolute and relative dosimetry due to the characteristics of small fields presented in the next paragraphs. (25, 26)

The small field can be defined by the following conditions:

1) Loss of a charged particle equilibrium on the beam axis
2) Partial occlusion of the primary photon source by the collimating devices on the beam axis.
3) The size of the detector is similar or large compared to the beam dimensions.

These conditions result in overlap between the field penumbrae and the detector volume. The field is considered as a small field, if at least one of these conditions apply. (25)

To measure the absorbed dose in a medium, a dosimeter have to be embedded into the medium. However, in most cases the sensitive medium of the dosimeter is not the same material as the measured medium. Cavity theory relates the absorbed dose in the dosimeter cavity to the absorbed dose in the measured medium. Bragg-Gary cavity theory provides a relationship between the absorbed dose in a dosimeter and the absorbed

dose in the medium containing the dosimeter. The Bragg-Gray cavity theory conditions are that the “cavity is small compared to the range of charged particle incident on it” and “the absorbed dose in the cavity is deposited solely by charged particles crossing it”. Under these conditions, the dose in the medium is related to the dose in the cavity by the ratio of the average unrestricted mass collision stopping powers of the medium and the cavity, according to the Bragg-Gray cavity theory. (27)

Secondary electrons with finite range are released through photon interactions in material. Secondary electrons contribute measurably to the absorbed dose. If the number of charged particles entering and leaving the volume is equal, the charge particle equilibrium occurs. The loss of lateral charged particle equilibrium occurs if the beam half width is smaller than the maximum range of the secondary electrons. As a result, the delivered dose to the active volume of the detector is unequal to the dose created by the same electrons from the opposite edge in the lateral direction. In case of small fields, the lateral range of electrons is usually larger than the field size. (25, 28)

The primary source of the treatment unit has a finite size. It is determined by the full width half maximum of the bremsstrahlung photon fluence distribution exiting the target. In case of the small field, the field collimation can shield the part of the finite primary photon source, producing a lower beam output compared to the unshielded situation of larger fields. The partial occlusion of the primary source has an influence on the particle spectrum as well as is a source of steep gradients in local absorbed dose. The both phenomena can have a significant effect on the detector response as well as cause a sharp drop in beam output as the field size decreases. The larger the energy or the smaller the density of the medium, the more pronounced the phenomenon. In case of the partially shielded primary source, the geometrical penumbra is extended all over the field cross section. This leads to the problem that the traditional field size determination based on full width at half maximum breaks down and underestimates the field size. In addition to these challenges, the characteristics of the MLC cause more challenges for the field size determination. (25, 26, 28)

The radiation detector in the radiation field produces a signal proportional to the mean absorbed dose over the sensitive volume of the detector. In case of the small radiation field size relative to the detector size, the inhomogeneity of the absorbed dose over the detector volume affects the signal received, as only a part of the detector volume is exposed to irradiation. This phenomenon is called volume averaging. As a result, the measured beam profiles are flattened: the dose in the field center is measured to be lower than actual, and the dose beyond the field edge is overestimated. In addition to the volume averaging, the presence of the detector causes the perturbation of the charged

particle fluence leading to the deviation from the Bragg-Gray cavity theory conditions. When the dose gradient is steep and there is a loss of the lateral charged particle equilibrium, these difficultly modelled fluence perturbations become large. (25, 26, 28)

In addition to the shielding of the primary photon source, the small field collimation decreases the amount of scattered radiation from the treatment head by shielding also the head scattered photons. As a result, low energy photons are absorbed by the collimators. In case of small fields, the amount of phantom scatter decreases compared to the conventional field sizes. This phenomenon of reduced phantom scatter is even more pronounced than the reduction of the head scatter. In combination, these two phenomena result in photon beam hardening increasing the average photon energy compared to the conventional fields. On the other hand, this beam hardening results in a change of the ratio of mass energy absorption coefficients as well as stopping-power ratio between water and the detector material. (25)

3.1.1 Relative dosimetry

The dosimetry of radiation therapy can be divided into two main categories, to relative dosimetry and absolute dosimetry. The absolute dosimetry covers only the dose calibration of treatment unit in water phantom with ionization chamber calibrated in standard dosimetry laboratory. All the other quality assurance measurements are relative to the absolute dose measurements. The relative dosimetry is independent of many correction factors required in absolute dosimetry, such as pressure-temperature correction and recombination correction, as the correction factors are not relative to the location of the detector in the radiation field. Instead, the measurement in one arbitrary point can be divided by the measurement in reference point and as a result, the relationship of absorbed doses in those points are defined. (13)

Nowadays each patient treatment plan is customized and unique. In IMRT/VMAT treatments each treatment field can be highly complex and QA is required to verify the treatment planning system's ability to calculate the dose accurately and to verify the ability of the treatment unit to deliver the planned dose accurately. In addition, the mechanical inaccuracies can lead in significant measurement errors. (13), (29)

The commissioning and QA of 3D-treatment planning system requires comparison of measured and calculated dose distributions. Dose distribution can be measured in a plane perpendicular to its axis or in a phantom. In this thesis we concentrate on measurements in a plane perpendicular to its axis. The measured dose distributions are compared with the predicted distributions from the treatment planning system. (12)

3.2 Gamma index analysis

Gamma index evaluation is a standard technique to quantitatively evaluate measured distributions against the dose distributions predicted by the treatment planning systems. The gamma analysis is needed for film, array dosimeter and portal dosimetry measurements as those measurement methods consists of multiple measurement points. The gamma index analysis combines the *dose difference* and the *distance to agreement* criteria to calculate a dimensionless metric for each point in the evaluated distribution. (30)

In low gradient regions, the doses can be compared directly. The acceptance tolerance is set for the difference between measured and calculated doses. On the other hand, in high dose gradient regions, a small spatial error can result in a large dose difference. In this case the dose difference is not a good measure of acceptability and distance-to-agreement (DTA) distribution is used to determine the acceptability of the dose calculations in high dose gradient regions. DTA is defined as a distance between a measured data point and the nearest calculated point in which the dose value is equal to that measured value. As a result, the dose difference and the DTA evaluations complement each other in the dose distribution analyses. (4)

An interpolation of the evaluated dose distribution is required for gamma analysis, when the measurements are widely spaced relative to the DTA criterion. A gamma value of <1 indicates that a point lies within the *dose difference* / *distance to agreement* passing criteria. Common passing criteria are, for example, 3%/3 mm and 2%/2 mm. In a quality assurance routine, the total percentage of points having gamma index <1 is calculated and a pass/fail threshold is set. A common passing threshold is 95%. (30)

The gamma value for the measured point r_m is defined by the following formulae:

$$\gamma(r_m) = \min\left\{\sqrt{\frac{|r_c - r_m|^2}{\Delta d_M^2} + \frac{[D_c(r_c) - D_m(r_m)]^2}{\Delta D_M^2}}\right\} \forall\{r_c\}$$

r_m position of a single measurement point

r_c spatial location of the calculated distribution relative to the measurement point

Δd_M passing criteria for isodose distance

ΔD_M passing criteria for dose

$D_c(r_c)$ calculated dose in r_c

$D_m(r_m)$ measured dose in r_m

The pass-fail criteria are:

$\gamma(r_m) \leq 1$ calculation passes

$\gamma(r_m) > 1$ calculation fails

This gamma calculation is performed for all r_m.

3.3 Point detectors

Point detectors allow absolute dose validation at individual points, but they are not suitable alone to the validation and QA of IMRT/VMAT dose distributions. However, array detectors based on single point detectors are suitable for IMRT/VMAT quality assurance.

3.3.1 Ionization chambers

An ionization chamber is a gas filled cavity surrounded by a conductive wall. The collecting electrode is placed in the center of the cavity and is separated from the wall with an insulator. The insulator and a guard electrode reduce the chamber leakage. Open air ionization chambers require temperature and pressure correction. An electrometer is required to measure small currents induced in the ionization chamber by ionizing radiation.

Cylindrical ionization chambers are the most common measurement device for point-dose measurements of photon radiation used in radiation therapy. The cylindrical ionization chambers exhibit excellent stability, small directional dependency, excellent linear response to absorbed dose, response independency of beam-quality and it is traceable to a primary calibration standard. The cylindrical symmetry minimizes the directional dependency when the beam central axis is perpendicular to the chamber axis of symmetry. Ionization chambers used for beam calibration are waterproof and designed with air-ventilation. (3)

Volume averaging is a character that the ionization chambers exhibit always to some extent. As a result, the effect is the most pronounced in the beam penumbra regions. For possible IMRT measurements, to minimize the volume averaging effect, the ionization chamber is recommended to be placed in the region of relatively homogenous fluence and in the regions of relatively homogenous dose in case of total dose measurements. The volume averaging effect is more pronounced in small treatment fields, as the size of the detector is large compared to the size of the field. (3)

Stem effect is an effect in which the irradiated portion of the ionization chamber stem can induce leakage current perturbing the collected charge. This phenomenon is more pronounced in small ionization chamber detectors, as the signal of these detectors is much weaker than signal of larger ionization chambers. (3)

3.4 Array detectors

Array detector is a dosimetric measurement device that comprises of a set of detectors, most commonly diode detectors or ionization chambers, placed in an array. The spacing between adjacent detectors define the spatial resolution of the device. In some array detectors, the spacing between detectors might be denser in the middle of the array and sparser in the outer parts of the array. To increase the spatial resolution, it might be possible to follow a measurement protocol in which the same treatment field is measured twice with a short offset in the array location to double the measurement points in the measurement area. Array detectors are calibrated to yield multiple cumulative reading of absorbed dose across a 2D plane to provide a large number of dose measurements in a single irradiation. The measurement results are available immediately. (3)

The array detectors are developed especially for the QA of treatment plans. 2D arrays can also be used to check the beam symmetry. The QA of treatment plans with array detectors is based on the comparison of measured and predicted/calculated dose. The most common analysis method for array measurements is the gamma analysis. In addition to the gamma analysis, the dose difference solely is of interest when comparing measured and predicted dose. In order to compare measured and calculated dose planes, the array detector needs to be calibrated with a known field size and dose to be able to measure absolute dose level of the measurement field. In 3D array detectors, the detectors are formed in a 3D planes. (3)

The 2D array detectors can be used as mounted in the gantry holder for IMRT measurements and for VMAT measurement, they can be either mounted on the gantry holder or placed on the treatment table with a certain buildup material/phantom. In case of the gantry holder, the beam is coming perpendicularly to the array surface independent of the gantry angle and the actual summation of 3D dose will stay unclear. In case that the array is located on the treatment table, the direction of irradiation reaching the detectors varies with the gantry angle. In such case, the angular dependency of the detectors needs to be taken into account. This method takes better into account the actual 3D summation of the dose. (3)

3.4.1 I'mRT MatriXX Evolution

I'mRT MatriXX Evolution 2D array device (IBA Dosimetry GmbH, Schrwarzenbruck, Germany), presented in the figure 4., consists of 1020 vented parallel ion chambers arranged in a 32 x 32 grid. The air in the ionizing chambers is ionized, when irradiated. The released charge is separated by the electrical field between the top and bottom electrodes. The electrical current is measured and digitized by a non-multiplexed 1020 channels current sensitive analog to digital converter. The active measurement area is 24.4 cm x 24.4 cm, and the chamber diameter is 4.5 mm and height 5.0 mm resulting in a chamber volume of 0.08 cm^3. The distance between adjacent chambers is 7.62mm measured from center to center. The OmniPro IMRT software enables 1 mm resolution with linear interpolation using low pass filter. The absorber thickness on top of the measurement device is 3 mm ABS Tecaran with density of 1.06 g/cm^3, resulting in water equivalent depth of 3.1 mm. The effective point of measurement is 3.5 mm below the surface and is indicated by engraved markers on the housing sides. (31)

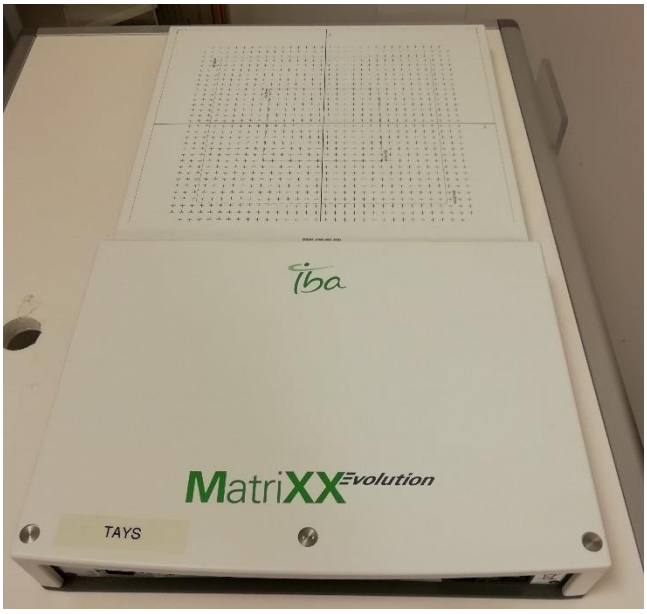

Figure 4. *I'mRT MatriXX Evolution array detector*

Saminathan et al. (32) evaluated the dosimetric characteristics of I'mRT MatriXX. The basic dosimetric evaluation included output factor, dose linearity and dose rate dependency. In addition, IMRT treatment plan measurements with I'mRT MatriXX were compared with film measurements. The response of the I'mRT Matrixx in dose measurements was linear for all the energies measured from 2 to 500 MU. The dose rate measurement proved the I'mRT MatriXX to be independent of dose rate between 100 MU/min to 600 MU/min for all the energies measured. The observed results were in close agreement with ion chamber measurements. These measurement proved that the device can be used for the measurements of dose gradients. The output measurements with I'mRT

MatriXX were in close agreement with the ionization chamber measurements (6 MV and 18 MV) and the parallel plate ionization chamber measurements. Discrepancies of ± 0.5% were found, resulting possibly from the scatter arising from the components of the array. Gamma analysis (3%/3 mm) revealed good agreement for test patterns and clinical treatment plans in I'mRT MatriXX and film measurements. They conclude that according to their measurements, the I'mRT MatriXX array detector can be used for quantifying absolute dose with the required accuracy level. (32)

3.5 Portal dosimetry

Varian linacs are equipped with EPIDs, which were originally designed for patient positioning as a MV imagers. kV- on board imagers have replaced the MV imagers as a patient positioning device due to their better soft tissue contrast. Due to EPIDs' high sensitivity, special resolution and immediate digital format, EPIDs have been utilized for patient plan quality assurance. (21)

The first commercial EPIDs were based on liquid-filled ionization chambers or cameras. Nowadays, the most commonly available EPIDs are active matrix flat panel imagers based on amorphous-silicon (aSi). The imager panel consists of an X-ray converter, a light detector, and a processing unit, hence the aSi EPID systems are based on indirect method. (24)

Figure 5. *Varian aS1200 EPID on Truebeam STx linac*

The scintillator converts the incident radiation into visible photons. The visible photons are sensed by an array of photodiodes in the amorphous silicon panel and they integrate the incoming light in an electric charge. The electrical charge is accumulated in the photodiode until the signal is read out and digitized. In Varian aS1200 EPID, presented in figure 5, the charge information is transferred to the readout electronics by activating the pixel matrix row by row while the columns are read out. The charge is converted into

digital form which results in a discrete value in each pixel. The TrueBeam system provides three MV image acquisition techniques triggered by the Supervisor: Single MV radshot for setup images, Synchronized MV for cine and single image acquisition and Unsynchronized MV for dosimetry. In dosimetry mode, dose/frame is kept constant by adapting frame rate. Varian aS1200 EPID is a matrix detector with resolution of 0.03 cm^2. The total sensitive area is 40 x 40 cm^2 with 1190x1190 pixel arrays, pixel pitch 0.336 mm. The aS1200 EPID is attached to the gantry through a robotic arm. A backscatter shielding is included in the cassette design to avoid the scattered radiation from the robotic arm. (21, 33)

EPIDs are quick and easy to use compared to the detector array measurements. They also enable finer spatial resolution compared to the array detectors. EPID enables measurements of single treatment fields in a perpendicular manner, as the EPID is mounted in the gantry opposite to the treatment head. A number of corrections needs to be applied to convert the signal detected by the EPID into the fluence or dose in the detector plane. The predicted calculated dose is typically determined at the plane of the detector as a portal dose image by the treatment planning system. (3)

Varian offers two algorithms with portal dose calculation capability for the aS1200 detector: Portal Dose Image Prediction (PDIP) and AAA. The portal dose measurements can be performed at any source to detector distance (SDD), but the optimum accuracy can be achieved by using a single SDD as close to the isocenter as possible for all the measurement steps (the calibration, configuration and portal acquisition).(34)

PDIP algorithm is a standalone algorithm which is configured independently of any other algorithms. It calculates the planned fluence by summing up the individual aperture fluences from control points of the field taking also into account the dynamic dose rate as well as the accumulated fluence between control points. The predicted portal dose image is determined at the EPID's detector plate ignoring the couch or the patient and the image is produced in terms of calibrated unit (CU). (5)

According to Varian Eclipse Photon and Electron Algorithms Reference Guide (34), PDIP calculates the portal dose image by convolving the fluence with Gaussian kernels as:

$$P = f' \times k \cdot \left(\frac{SAD}{SDD}\right)^2 \left(\frac{OF(fs_x, fs_y)}{PSF(fs_x, fs_y)}\right)$$

where

$P =$	Calculated portal dose image in terms of CU
$f' =$	Input fluence corrected by the intensity profile and scaled by detector distance
$\times =$	Convolution operator
$k =$	Portal imager dose kernel
$SDD =$	Source-to-detector distance of the portal image measurement
$SAD =$	Source-to-axis distance of the treatment unit
$fs_x =$	Field size at the SAD in the FX-direction
$fs_y =$	Field size at the SAD in the FY-direction
$PSF(fs_x, fs_y) =$	Phantom scatter factor for field size fs_x, fs_y, defiend at SAD
$OF(fs_x, fs_y) =$	Output factor for field size fs_x, fs_y, defiend at SAD and normalized to a 10x10 cm^2 field in terms of CU

(34)

The AAA can be used for portal dose calculation with the same configured beam data as used for patient dose calculation. However, currently AAA can be used only for portal dose calculation of 6 FFF beams and for the aS1200 detector. A portal image is calculated in terms of CU at the detector aS1200 plate, ignoring the treatment couch and the patient. The AAA performs the dose calculation with an internal model of the aS1200 detector. In order to predict the appropriate dose response of the detector, the algorithm uses scatter kernels calculated in the imager scintillator material. (34)

For portal dosimetry, the EPID is working on the dosimetric mode acquiring image frames during irradiation. The irradiation happens undisturbed, as there is no synchronization between linac and EPID. Previously, the problem has been that the high dose rate of FFF-beams led to a saturation of EPID and to the loss of information, as the amount of

radiation was too high between two frames. In aS1200 EPID, this problem has been solved. (12)

The calibration of EPID is required regularly. The calibration procedure includes the following steps: dark field, flood field, pixel defect map and absolute dose calibration. The SDD for calibration process with Varian TrueBeam system is 100 cm. The dark field is an acquisition without radiation. The flood field is an acquisition of a field covering the whole detector plate. The pixel defect map is computed based on the dark and the flood fields, and is corrected by averaging the neighboring pixels. The absolute dose calibration is performed by irradiating a 10 x 10 cm^2 field with a known number of MUs, assigned to Calibration Units (CU), for all the energies needed for portal dosimetry.(12)

Miri et al. (21) performed a basic dosimetry commissioning on the aS1200 EPID and TrueBeam 2.0 linac for flattened (FF) and FFF bams. Dosimetry testing included tests for linearity of dose response with MU, imager lag and effectiveness of backscatter shielding. The dose linearity of the EPID was within 0.4% above 5 MU and 1% above 2 MU. The imager lag was extremely small compared with previous EPID versions and no increase in image signal with MU was found. The symmetry of the beam profiles for EPID was considerably improved from the previous EPID models, proving the backscatter shielding to be effective in the aS1200 EPID model. These results suggest that the aS1200 has excellent dosimetric properties compared to the previous EPID models. (21)

4. MATERIALS AND METHODS

All the verification plans were delivered on a Varian TrueBeam™ STx accelerator equipped with a high-definition multileaf collimator HD120™ intended for stereotactic treatments and aS1200 electronic portal imaging device. The 32 central leaf pairs spanning 8 cm are 2.5 mm wide (projected at isocenter) and the outer leaf pairs spanning outer 14 cm 5 mm wide (projected at isocenter), the total number of leaves being 120. The radius of curvature of rounded leaf ends is 16 cm.

4.1 Treatment plan selection

For this retrospective study, 48 treatment plans were selected from three different target sites (20 brain, 19 lung and 9 prostate tumors), previously treated in TAUH. Single target plans were chosen to be evaluated to avoid convolving issues due to multiple targets. All the treatment plans were planned according to the clinical protocol of stereotactic treatments, carried out with VMAT technique applying FFF beams. Treatment plans included in this study comprise comprehensive set of typical clinical cases from each target site group with most typical fractionation schemes. All the treatment plans were generated using Eclipse treatment planning system version 13.6. Dose calculation algorithm was AAA (version 13.6.23) and calculation grid was isotropic 1.0 mm for brain and lung tumors, and 2.5 mm for prostate tumors. Box plot-distributions for planning target volumes (PTV) of different target sites are presented in figure 6A. Figure 6B. presents distributions of PTV volumes treated with 6 FFF and 10 FFF energies. Figure 6C. presents the distributions of MU/Gy. Treatment plan properties including number of patients, fractionation schemes, energy, volume of PTV, number of VMAT arcs and MU/Gy are presented in table 1.

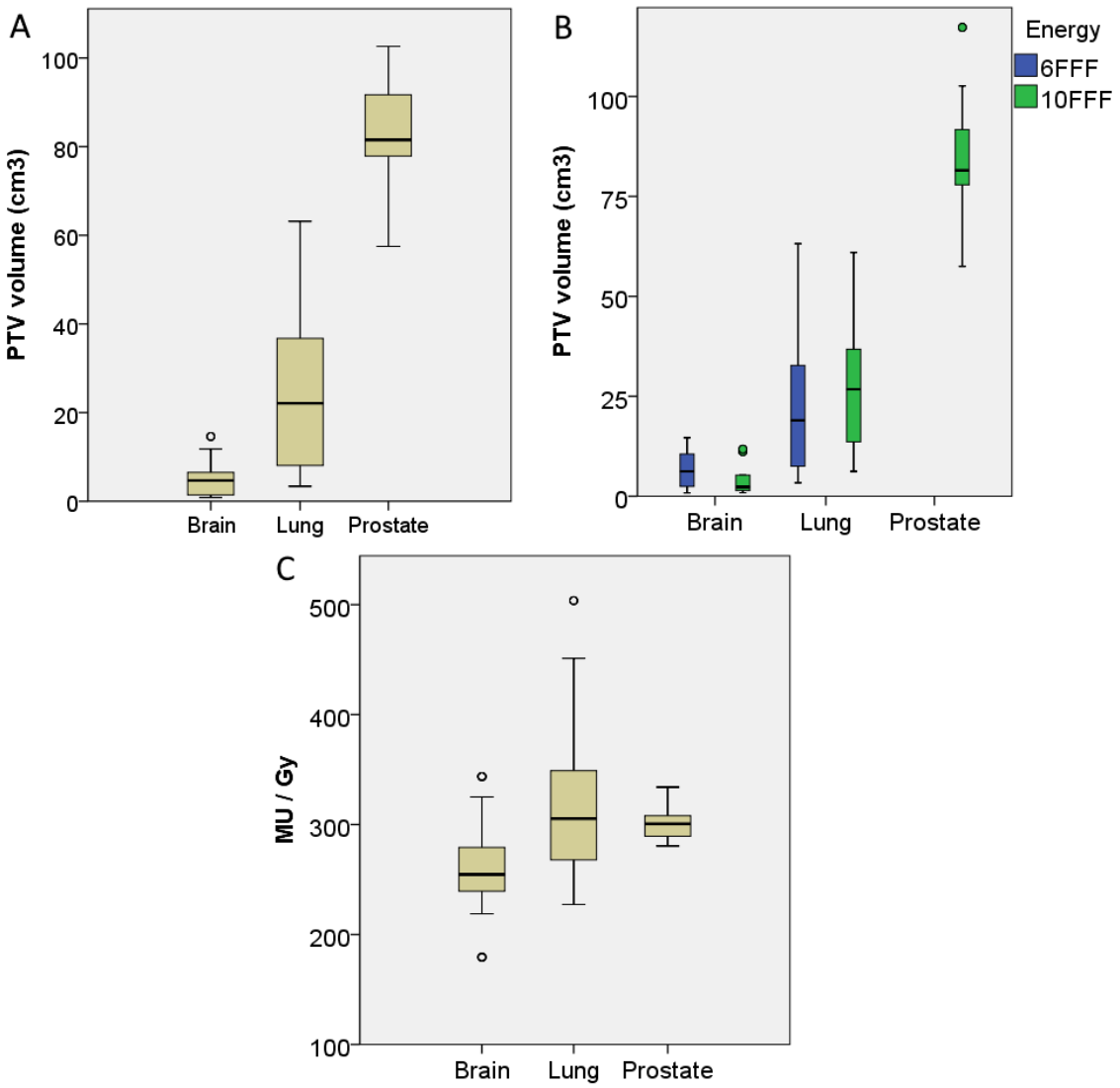

Figure 6. *Box plot distributions of (A) PTV volumes, (B) PTV volumes treated with 6 FFF and 10 FFF energies and (C) MU / Gy in categories of brain, lung and prostate tumors.*

Table 1. *Treatment plan properties*

Treatment site	No. of patients	Fractionation	Energy	Volume of PTV (cm^3)		No. of VMAT arcs		MU/Gy
Brain	20	4	1x20Gy	Mean 5.39 SD 4.27 Min 0.83 Max 14.63	Mean 6.39 SD 4.5 Min 0.83 Max 14.63	2-3	Mean 260.6 SD 37.2 Min 179.4 Max 343.7	Mean 266.8 SD 50.2 Min 179.4 Max 343.7
		3	3x 9Gy			3-4		
		3	5x 6Gy			2		
		3	1x20Gy		Mean 4.40 SD 4.0	2		Mean 254.3 SD 17.75
		4	3x 9Gy		Min 0.88	2-3		Min 237.7
		3	5x 6Gy		Max 11.79	2		Max 295.0
Lung	19	2	3x18Gy	Mean 25.32 SD 18.6 Min 3.37 Max 63.17	Mean 22.74 SD 19.3 Min 3.37 Max 63.17	2	Mean 319.7 SD 70.9 Min 227.2 Max 503.7	Mean 340.8 SD 86.35 Min 243.3 Max 503.7
		6	5x11Gy			2		
		2	8x7.5Gy			2		
		1	3x18Gy		Mean 28.2 SD 18.4	2		Mean 296.2 SD 41.84
		6	5x11Gy		Min 6.21	2		Min 227.24
		2	8x7.5Gy		Max 60.97	2		Max 353.75
Prostate		9	5x 7.25/7Gy		Mean 84.8 SD 18.1 Min 57.5 Max 117.3	2		Mean 303.8 SD 18.9 Min 280.6 Max 334.0

4.1.1 Brain tumors

Fractionation schemes in treatment plans measured in this thesis for brain tumors were 1x 20 Gy, 3x 9 Gy and 5x 6 Gy. Target volumes ranged from 0.83 cm^3 to 14.63 cm^3. 6 FFF (dose rate 1400 MU/min) and 10 FFF (dose rate 2400 MU/min) beam energies were used. The number of VMAT arcs was 2-4 per treatment. Depending on the tumor location, either full arcs or partial arcs were used. VMAT optimization algorithm was PRO (version 11.0.31). An example of a typical treatment plan setting for a brain tumor is presented in the Appendix A.

4.1.2 Lung tumors

Fractionation schemes in treatment plans measured in this thesis for lung tumors were 3x 18 Gy, 5x 11 Gy and 8x 7.5 Gy. Target volumes ranged from 3.37 cm^3 to 63.17 cm^3. 6 FFF (dose rate 1400 MU/min) and 10 FFF (dose rate 2400 MU/min) beam energie were used. The number of VMAT arcs was 2-3 per treatment. Depending on the tumor location, either full arcs or partial arcs were used. VMAT optimization algorithm was PRO (version 11.0.31). An example of a typical treatment plan setting for a lung tumor is presented in the Appendix B.

4.1.3 Prostate tumors

Fractionation scheme in treatment plans measured in this thesis for prostate cancer was extreme hypofractionation scheme 5x 7.25/7 Gy. The region of prostatic urethra received 7 Gy while the rest of the prostate PTV received 7,25 Gy using simultaneous-integrated boost technique. Clinical target volume (CTV) was the prostate and PTV was formed from the CTV adding 3mm margin posteriorly and 5mm elsewhere. The treatment technique was VMAT. Target volumes ranged from 57.49 cm^3 to 117.27 cm^3. 10 MV FFF (dose rate 240 0MU/min) beams was used. The number of VMAT arcs was 2 per treatment. Two full were used. VMAT optimization algorithm was PO (version 13.6.23). An example of a typical treatment plan setting for a prostate tumor is presented in the Appendix B.

4.2 Analysis criteria

4.2.1 Gamma analysis

The gamma analysis was performed for both portal and array measurements. The gamma passing rates for the following gamma criteria (*dose difference* / *distance to agreement*) were calculated: 3%/3 mm, 2%/2 mm, 1%/1 mm and 3%/1 mm.

Two threshold values were used: 5% and 60%. The threshold value determines the dose level included in the gamma evaluation: the pixels receiving dose less than the threshold value of the maximum dose were not included in the gamma evaluation. The threshold of 5% from the maximum dose removes the noise from the analysis, but the dose due to leakage radiation between MLC leaves is taken into account. The threshold of 60% from the maximum dose removes also the dose due to the leakage radiation. The passing rates for gamma values <1 were calculated indicating the points lying within the given dose value difference and distance to agreement criteria.

4.2.2 Average percentual dose difference analysis

The average percentual dose differences with the same threshold values as in the gamma evaluation (5% and 60%) were analyzed from the portal dose images by the following formula:

$$Average\ percentual\ dose\ difference = \frac{Average\ dose\ difference\ (CU)}{Maximum\ CU\ in\ predicted\ image}.$$

Negative average percentual dose difference values indicate that the measured dose is smaller than the predicted dose.

OmniPro-analysis software does not have a threshold tool for dose difference measurements, so the average percentual dose differences could not be measured for the array measurements.

4.3 Quality assurance of treatment plans with portal dosimetry

The verification plan creation was performed in the Eclipse treatment planning system. Source-Imager distance (SID) for calculated image was 100 cm. The verification plans were created using the actual planned gantry angles (GA) and collimator angles (CA). The predicted images were calculated using the PDIP-algorithm (version 13.6.23).

The portal dosimetry system was calibrated according to manufacturer instructions before the measurements. SID was 100 cm both in calibration and measurements. For measurements, the treatment couch top was removed and the GAs and CAs were the same as in the treatment plans to simulate the gravitational effects. The couch rotations were not included, as the portal imager has a fixed geometry with the gantry. The measurement set up is presented in the figure 7. All the plans were delivered with the planned dose rate of 1400 MU/min (6 FFF) or 2400 MU/min (10 FFF).

Figure 7. *Portal dose measurement set up*

The analysis of measured and predicted dose distributions was performed in the *Portal Dosimetry* –workspace. Measured and predicted images were aligned automatically before the analysis. The dose region for gamma analysis can be defined in *Portal Dosimetry* -workspace by two parameters: Region of interest (ROI) and threshold. In this study, only a threshold was used. All the verification plan fields were analyzed.

4.4 Reference calculation for portal dosimetry with AAA

In Eclipse version 15.5, AAA-algorithm (version 15.6.03) is configured also for portal dose calculation for 6 FFF beams in combination with the aS1200 electronic portal imaging device. All the treatment plans with 6 FFF energy (10 brain and 10 lung treatment plans) were recalculated for portal dosimetry with AAA-algorithm, re-measured and analyzed with the same protocol presented in the chapter 4.3 to compare the validity of AAA algorithm in comparison with the PDIP algorithm.

4.5 Quality assurance of treatment plans with I'mRT MatriXX Evolution array detector

The I'mRT MatriXX Evolution measurement work flow consists of a creation of reference dose distributions in the I'mRT MatriXX Evolution geometry, calibration of the array, measurements, and analysis of measured and predicted dose distributions with dedicated software (OmniPro I'mRT System Version 1.7b).

The reference dose distributions were calculated in the Eclipse treatment planning system with AAA (version 13.6.23). The GAs and CAs were the same as in the treatment plans. Each field was placed into a separate verification plan. The isocenter was placed in the surface of the I'mRT MatriXX Evolution detector and in the middle of the detector area, as is the case in the measurements. The reference dose distributions were exported to the OmniPro-software.

Figure 8. *I'mRT Matrixx Evolution measurement set up. The array detector was placed on the gantry holder with SSD 100 cm and 5 cm of water equivalent build-up material was set above the detector.*

The measurement setup for I'mRT MatriXX Evolution is presented in the figure 8. The ionization chamber array was placed in the gantry holder with source to surface distance (SSD) of 100 cm for the measurements. 5 cm of water equivalent build-up material was placed above the detector. The array system underwent a 60-min warm up- time with power on and preirradiation with 800 MUs with 27 x 27 cm^2 field size before the measurements. After the preliminary irradiation, the background radiation was measured. The

calibration for absolute measurements were performed according to the manufacturer's instructions. The calibration with 10 x 10 cm^2 field size and 100 MU was based on the measurement values obtained from the four center chambers with reference doses of $D_{ref(6FFF)}$ = 0.914 Gy for 6 FFF and $D_{ref(10FFF)}$ = 0.982 Gy for 10 FFF beams.

The treatment plans were irradiated in the QA mode of the linac and each arc was measured separately. The measurements were analyzed with OmniPro analysis software. The calculated dose distribution data was converted at first into measurement resolution of 0.7619 cm, and then to the 0.1 cm resolution. The measured data was converted to the 0.1 cm resolution. Synchronized rescaling with maximum dose to 100% was used. The alignment of the measured and calculated dose distributions was performed manually, as an automatic tool is not available in the software.

4.6 Statistical methods

The statistical tests were carried out using the IBM SPSS Statistics version 22.

Normality of the data was tested with Shapiro-Wilk test as it is recommended test in the SPSS software for sample size of less than 50. (35) Tests for inferential statistics were chosen based on the normality test results (parametric or non-parametric tests).

Correlations were obtained using Spearman's Rho, as the most data sets were non-normally distributed, according to the Shapiro-Wilk test. The Spearman's Rho is a non-parametric test used to measure the degree of association between two variables. The significance level of the correlation coefficient indicates the statistical significance of the coefficient. (36)

In this thesis, the correlation is considered

- weak, if the correlation coefficient is < 0.3
- moderate, if the correlation coefficient is 0.3 - 0.7
- strong, if the correlation coefficient is 0.7 - 0.9
- very strong, if the correlation coefficient is > 0.9

for statistically significant ($p < 0.05$) correlation coefficients.

The independent samples tests used were the Mann-Whitney U Test (for 2 samples) and Kruskal-Wallis 1-way ANOVA (for 2-3 samples), as the most data sets were non-normally distributed, according to the Shapiro-Wilk test. Independent samples tests were used to evaluate the similarity of the distributions of two or three categories (36). Gamma passing

rates and average percentual dose differences in categories of *brain/lung/prostate*, *6 FFF / 10FFF* as well as *PDIP/AAA/I'mRT MatriXX Evolution* were compared.

The paired samples test used was the Wilcoxon's signed rank test, as the most data sets were non-normally distributed, according to the Shapiro-Wilk test. Wilcoxon's signed rank test is a non-parametric analog to the pared Student's t-test when the sample size is small and non-normally distributed. It determines whether two dependent samples are selected from the populations having the same distribution. (36) Gamma passing rates and average percentual dose differences were tested pairwise with Wilcoxon's signed rank test between 6 FFF and 10 FFF, 5% threshold and 60% threshold, PDIP and AAA, PDIP and I'mRT MatriXX Evolution, as well as AAA and I'mRT MatriXX Evolution.

Box plots for PTV volume, MU/Gy, gamma passing rates and average percentual dose differences were drawn. Thick line in the middle represents the median. The top and bottom boxes show the 75^{th} and the 25^{th} percentiles. Whiskers show the maximum and the minimum values, with the exceptions of outliers represented by circles and extremes represented by asterisks. (37)

The p-value gives the probability that the two compared variables are from the same distribution with equal median. The significance level in this thesis was set to 0.05.

5. RESULTS

5.1 Gamma analysis

5.1.1 Portal dosimetry with PDIP-algorithm

Results and statistics of portal dosimetry measurements with PDIP-algorithm for brain, lung and prostate tumors are presented in the following paragraphs.

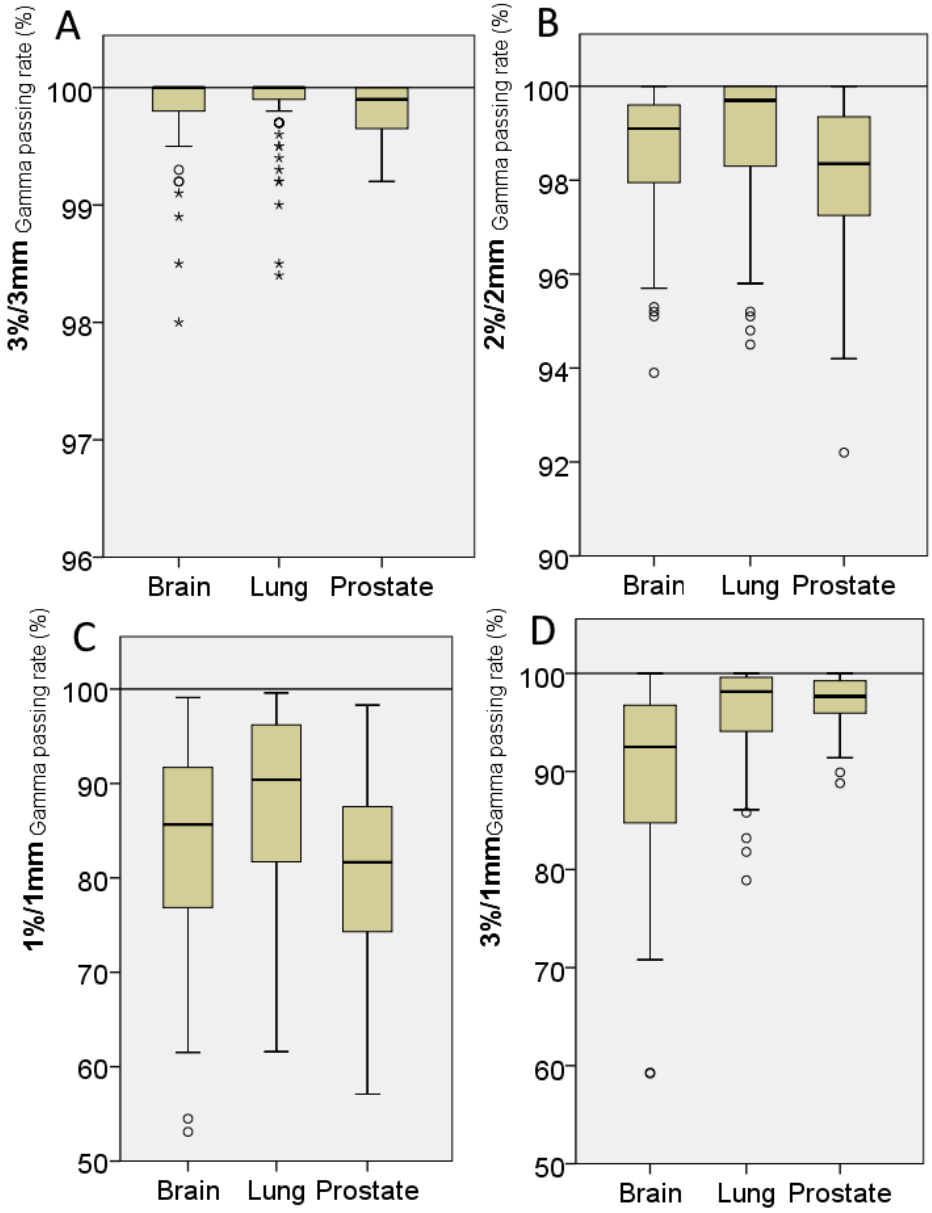

Figure 9. *Box plot –distributions of gamma passing rates for portal dosimetry measurements with PDIP-algorithm. Distributions are presented for brain, lung and prostate tumors with gamma criteria of 3%/3 mm (A), 2%/2 mm (B), 1%/1 mm (C) and 3%/1 mm (D).*

Figure 9. presents the box plot distributions of gamma passing rates with gamma criteria of 3%/3 mm, 2%/2 mm, 1%/1 mm and 3%/1 mm for categories of brain, lung and prostate tumors. According to the visual inspection of the distributions, the mean size of the target (brain 5.4 ± 4.3 cm^3, lung 25.3 ± 18.6 cm^3, prostate 84.8 ± 18.1 cm^3) do not seem to have an predictable effect on gamma passing rates with gamma criteria of 3%/3 mm, 2%/2 mm, 1%/1 mm. In case of gamma criteria of 3%/1 mm, the deviation decreases, as the mean target size increases.

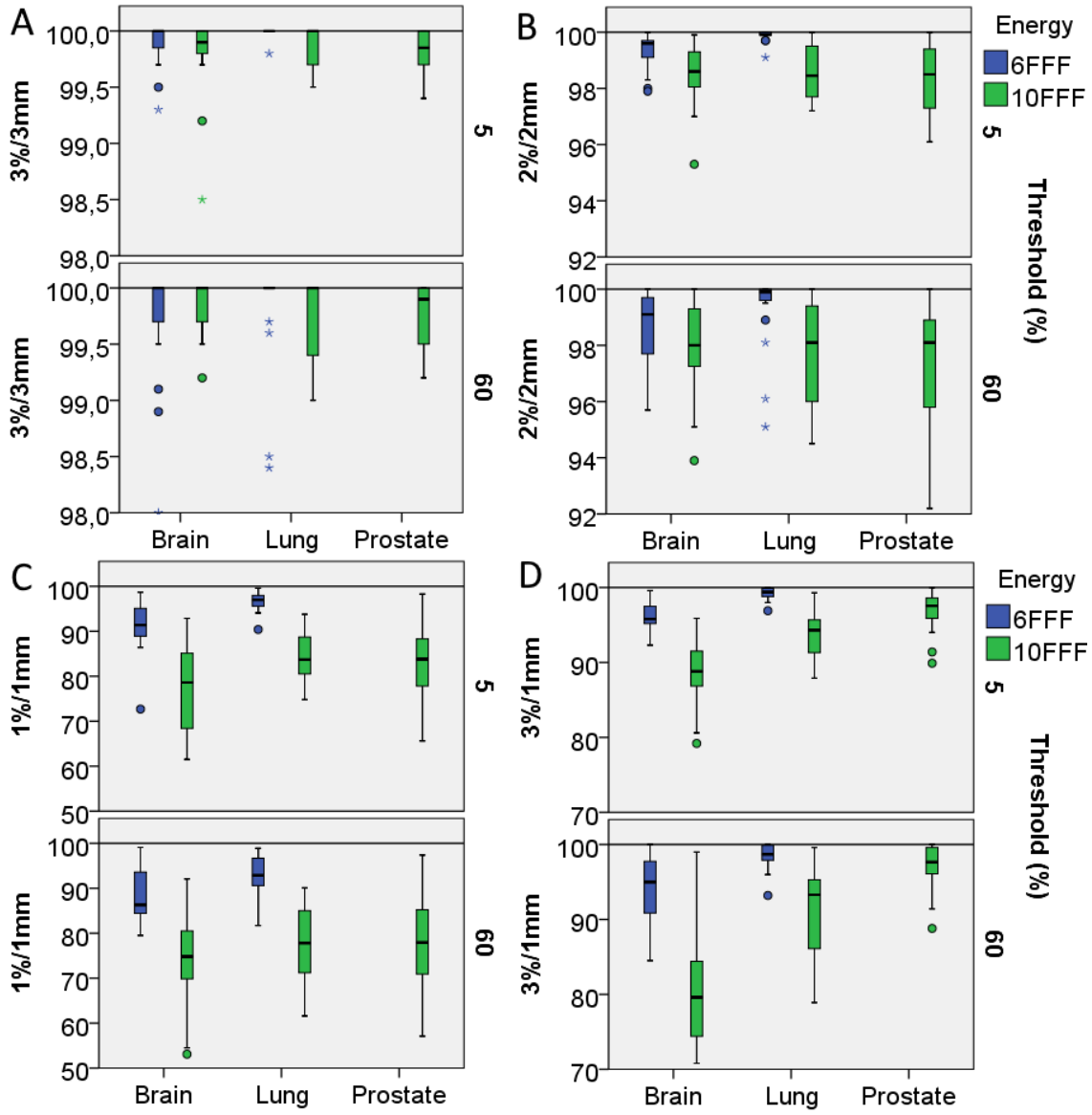

Figure 10. *Box plot –distributions representing the effects of energy (6 FFF and 10 FFF) and threshold (5% and 60%) to gamma passing rates of portal dosimetry measurements with PDIP-algorithm. Distributions are presented for brain, lung and prostate tumors with gamma criteria of 3%/3 mm (A), 2%/2 mm (B), 1%/1 mm (C) and 3%/1 mm (D).*

Figure 10. presents more detailed box plot -distributions of PDIP gamma analysis results with gamma analysis thresholds of 5% and 60%, and energies of 6 FFF and 10 FFF.

According to the visual inspection of the distributions, the gamma analysis results for 10 FFF beams result in lower gamma passing rates and increased deviations. Also threshold of 60% results in lower gamma passing rates and increased deviations, compared with threshold of 5%.

Table 2. presents the descriptive statistics (mean, SD) and Independent-Samples Kruskal-Wallis Test results for brain, lung and prostate tumors. Visual observations can be supported by the descriptive statistics in the Table 2. Independent-Samples Kruskal-Wallis tests reveal that as the gamma criteria tightens, significant differences between target site groups (brain, lung, prostate) increase. With gamma criterion of 3%/3 mm, only 6 FFF with 5% threshold reveals significant difference. With gamma criterion of 1%/1 mm, 6 FFF with 5% or 60% thresholds and 10 FFF with 5% threshold reveal significant differences. Gamma criterion of 3%/1 mm reveals significant differences in all categories.

Table 2. *Descriptives and Independent-Samples Kruskal-Wallis Test results in categories of brain, lung and prostate tumors for portal dosimetry gamma passing rates with PDIP-algorithm.*

			Brain	Lung	Prostate	Independent-Samples Kruskal-Wallis Test
		Energy	Mean ± SD	Mean ± SD	Mean ± SD	(Sig.)
PTV volume (cm3)		6FFF	6.08±4.28	23.22±18.48		0.000
		10FFF	4.18±3.70	28.18±17.83	84.80±17.56	0.000
MU/Gy		6FFF	267.4±50.7	339.9±82.0		0.002
		10FFF	253.53±16.74	296.15±40.59	303.79±18.29	0.000
		Threshold				
3%/3mm	6FFF	5 %	99.91±0.17	99.99±0.04		0.029
		60 %	99.77±0.46	99.82±0.47		0.239
	10FFF	5 %	99.82±0.34	99.87±0.16	99.83±0.18	0.713
		60 %	99.82±0.24	99.74±0.36	99.74±0.29	0.535
2%/2mm	6FFF	5 %	99.34±0.58	99.88±0.20		0.000
		60 %	98.65±1.32	99.34±1.34		0.007
	10FFF	5 %	98.53±1.07	98.57±0.93	98.47±1.13	0.982
		60 %	97.93±1.64	97.72±1.91	97.4±2.09	0.732
1%/1mm	6FFF	5 %	91.11±5.06	96.63±2.12		0.000
		60 %	88.62±5.85	92.95±4.70		0.016
	10FFF	5 %	77.68±8.90	84.25±5.05	83.22±8.40	0.047
		60 %	75.02±9.61	77.30±8.70	78.52±10.55	0.567
3%/1mm	6FFF	5 %	96.20±1.92	99.23±0.83		0.000
		60 %	93.93±4.96	98.50±1.76		0.000
	10FFF	5 %	88.68±4.57	93.69±3.55	96.82±2.80	0.000
		60 %	79.99±10.32	91.23±6.34	96.93±3.21	0.000

Independent-Samples Kruskal-Wallis Test null hypothesis:
The distribution is the same across categories of Brain/Lung/Prostate.

Table 3. presents Independent Samples Mann-Whitney U test results and correlations from energy comparison of treatment plans executed with 6 FFF or 10 FFF beam energies. Independent-Samples Mann-Whitney U Test reveals that in case of brain tumors, there is no significant difference between energies with gamma criteria of 3%/3 mm, but with tighter criteria, significant differences occur. In case of lung tumors, there are significant differences between energies with all gamma criteria. Portal dosimetry with PDIP-algorithm results with higher gamma passing rates for 6 FFF beams compared to 10 FFF beams. Spearman's correlations reveal that energy has a moderate correlation with gamma criteria of 2%/2 mm, 1%/1 mm and 3%/1 mm in case of brain tumors. In case of lung tumors, gamma criterion of 2%/2 mm correlate moderately, and gamma criteria of 1%/1 mm and 3%/1 mm correlate strongly with energy.

Table 3. *Independent Samples Mann-Whitney U test results and correlations with energy for portal dosimetry gamma passing rates with PDIP-algorithm in categories of brain and lung tumors.*

	Brain		**Lung**	
	Independent-Samples Mann-Whitney U Test (Sig.)	**Correlations with *energy*: Spearman's Rho (Coef./Sig.)**	**Independent-Samples Mann-Whitney U Test (Sig.)**	**Correlations with *energy*: Spearman's Rho (Coef./Sig.)**
3%/3mm	0.115	-0.159/0.115	0.005	-0.323/0.004
2%/2mm	0.001	-0.329/0.001	0.000	-0.645/0.000
1%/1mm	0.000	-0.685/0.000	0.000	-0.803/0.000
3%/1mm	0.000	-0.654/0.000	0.000	-0.727/0.000

Independent-Samples Mann-Whitney U Test Null Hypothesis:
The distribution is the same across categories of 6FFF/10FFF.

Table 4. presents results from Paired Samples Wilcoxon Signed Ranks tests and Spearman's correlations for gamma passing rates with thresholds of 5% and 60%. The paired sample test results reveal that when comparing pairwise the results with 5% threshold and 60% threshold, significant differences occur. Brain tumors treated with 10 FFF do not reveal significant differences, but all the other tumor sites and energies reveal significant threshold dependency. Spearman's correlations reveal that gamma passing rates with different thresholds correlate very strongly in brain 6 FFF 3%/3 mm, 6 FFF 2%/2 mm, 6 FFF 3%/1 mm, as well as in lung 10 FFF 3%/3 mm and 10 FFF 3%/3 mm. Gamma passing rates with different thresholds correlate strongly in brain 10 FFF 3%/3 mm, 10 FFF 1%/1 mm, as well as in lung 10 FFF 3%/3 mm and 10 FFF 3%/1 mm. Gamma passing rates with different thresholds correlate moderately in brain 10 FFF 2%/2 mm, 6

FFF 1%/1 mm and 10 FFF 1%/1 mm, as well as in lung 6 FFF 2%/2 mm, 6 FFF 1%/1 mm and 6 FFF 3%/1 mm.

Table 4. *Paired Sample Wilcoxon Signed Ranks test results and Spearman's correlations for gamma analysis threshold comparisons for portal dosimetry with PDIP-algorithm.*

		Brain		Lung		Prostate	
		Wilcoxon Signed Ranks Test (5%PDIP vs. 60%PDIP) (Sig.)	**Spearman's Rho (5%PDIP vs. 60%PDIP) (Coef./Sig.)**	**Wilcoxon Signed Ranks Test (5%PDIP vs. 60%PDIP) (Sig.)**	**Spearman's Rho (5%PDIP vs. 60%PDIP) (Coef./Sig.)**	**Wilcoxon Signed Ranks Test (5%PDIP vs. 60%PDIP) (Sig.)**	**Spearman's Rho (5%PDIP vs. 60%PDIP) (Coef./Sig.)**
3%/3mm	6FFF	0.005	0.929/0.000	0.068	0.377/0.092		
	10FFF	0.580	0.827/0.000	0.029	0.936/0.000	0.036	0.781/0.000
2%/2mm	6FFF	0.000	0.959/0.000	0.023	0.622/0.003		
	10FFF	0.063	0.663/0.001	0.008	0.863/0.000	0.001	0.950/0.000
1%/1mm	6FFF	0.011	0.693/0.000	0.000	0.551/0.010		
	10FFF	0.171	0.617/0.002	0.001	0.763/0.000	0.000	0.953/0.000
3%/1mm	6FFF	0.004	0.914/0.000	0.026	0.503/0.020		
	10FFF	0.000	0.789/0.000	0.006	0.962/0.000	0.587	0.926/0.000

5.1.2 Portal dosimetry with AAA-algorithm

Results and statistics applied by portal dosimetry with AAA-algorithm for brain and lung tumors are presented in the following paragraphs.

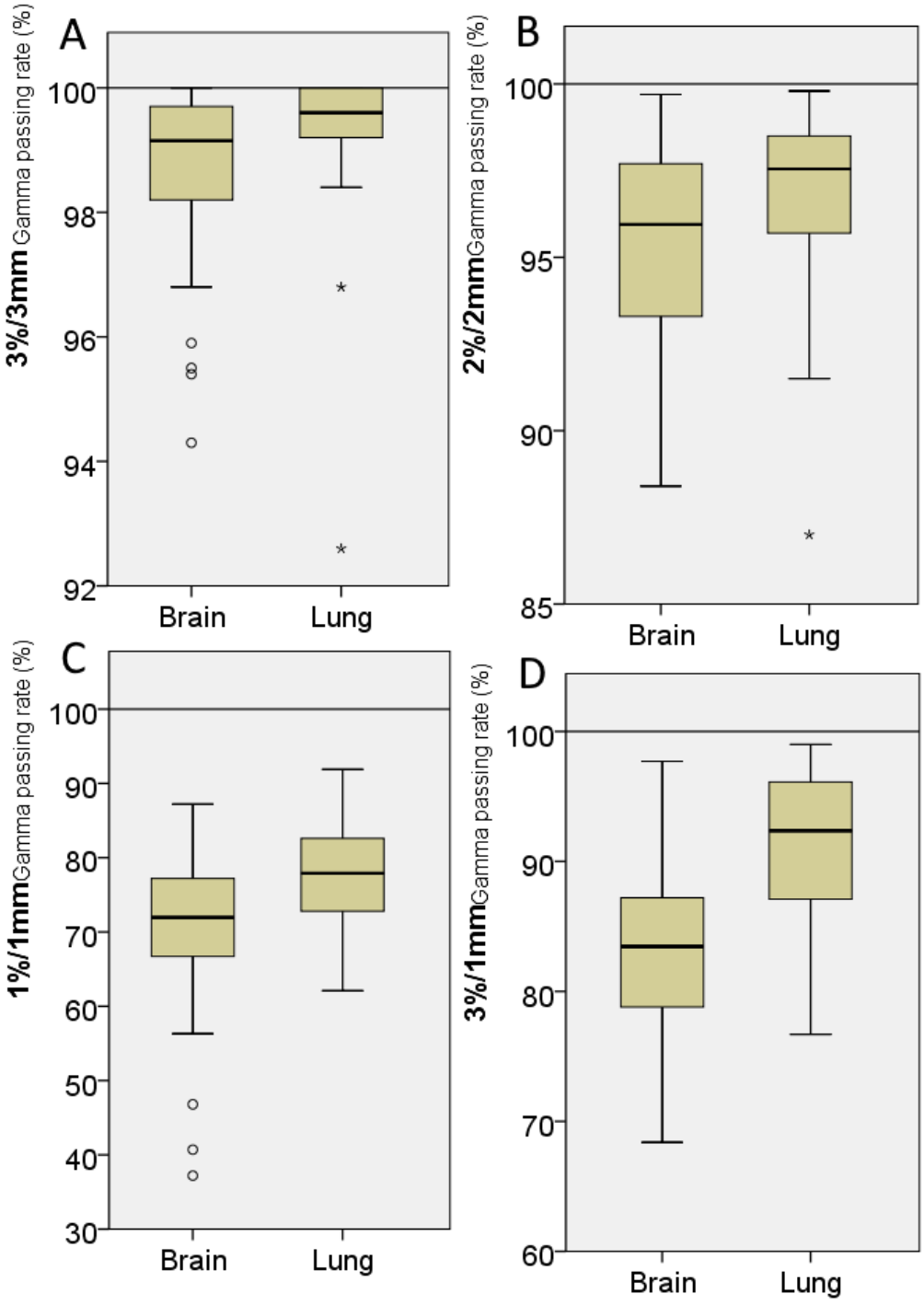

Figure 11. *Box plot –distributions of gamma passing rates for Portal dosimetry measurements with AAA-algorithm. Distributions are presented for brain and lung tumors with gamma criteria of 3%/3 mm (A), 2%/2 mm (B),1%/1 mm (C) and 3%/1 mm (D).*

Figure 11. presents the box plot distributions of gamma passing rates with gamma criteria of 3%/3 mm, 2%/2 mm, 1%/1 mm and 3%/1 mm for categories of brain, lung and

prostate tumors. According to the visual inspection of the distributions, the mean size of the target (brain 5.4 ± 4.3 cm^3, lung 25.3 ± 18.6 cm^3) has a noticeable effect on gamma passing rates with all gamma criteria. The gamma passing rates seem to increase and deviations decrease, as the mean target size increases.

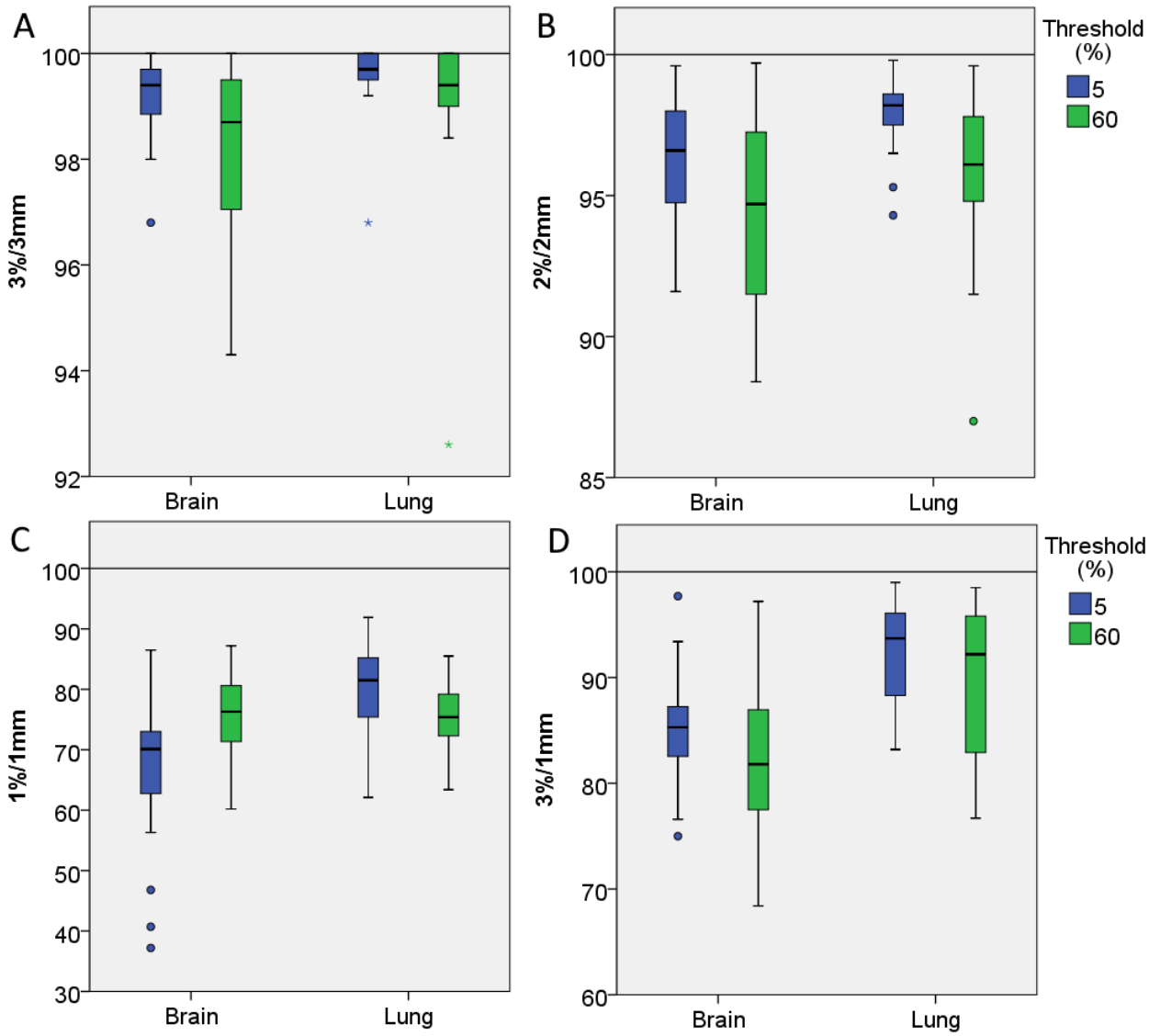

Figure 12. *Box plot –distributions representing the effect of threshold (5% and 60%) to gamma passing rates of portal dosimetry measurements with AAA-algorithm. Distributions are presented for brain and lung tumors with gamma criteria of 3%/3 mm (A), 2%/2 mm (B),1%/1 mm (C) and 3%/1 mm (D).*

Figure 12. presents more detailed box plot distributions of AAA gamma analysis results with gamma analysis thresholds of 5% and 60%. According to the visual inspection of the distributions, the gamma analysis results with threshold of 60% results in lower gamma passing rates and increased deviations in comparison with the results with threshold of 5%.

Table 5. presents the descriptive statistics (mean, SD) and Independent-Samples Kruskal-Wallis Test results for brain, lung and prostate tumors. Visual observations about the effect of threshold can be supported by the descriptive statistics. Independent-Samples Kruskal-Wallis tests reveal significant differences between target site groups (brain, lung) in all the other categories but not in 60% 2%/2 mm or 60% 1%/1 mm.

Table 5. *Descriptives and Independent-Samples Kruskal-Wallis Test results in categories of brain, lung and prostate tumors for portal dosimetry gamma passing rates with AAA-algorithm.*

		Energy	Brain Mean ± SD	Lung Mean ± SD	Independent-Samples Kruskal-Wallis Test
PTV volume (cm3)		6FFF	6.08±4.28	23.22±18.48	0.000
MU/Gy		6FFF	267.4±50.7	339.9±82.0	0.002
The shortest distance to the skin surface (cm)		6FFF	3.69±1.45	7.82±2.12	0.000
		Threshold			
3%/3mm	6FFF	5 %	99.18±0.76	99.57±0.68	0.012
		60 %	98.22±1.64	99.14±1.58	0.019
2%/2mm	6FFF	5 %	96.34±2.28	97.93±1.36	0.009
		60 %	94.33±3.68	95.90±2.82	0.173
1%/1mm	6FFF	5 %	67.23±11.49	80.04±7.03	0.000
		60 %	75.71±7.05	75.38±5.96	0.868
3%/1mm	6FFF	5 %	84.63±4.86	92.55±4.85	0.000
		60 %	81.61±7.25	89.37±7.57	0.002

Independent-Samples Kruskal-Wallis Test null hypothesis:
The distribution is the same across categories of Brain/Lung/Prostate.

Table 6. presents results from Paired Sample Wilcoxon Signed Ranks tests and Spearman's correlations for gamma passing rates with thresholds of 5% and 60%. The paired sample test results reveal that when comparing pairwise the results with 5% threshold and 60% threshold, significant differences occur for both tumor sites (except brain 1%/1 mm). Spearman's correlations reveal that gamma passing rates with different thresholds correlate very strongly in brain 3%/3 mm, lung 2%/2 mm and lung 3%/ 1mm, strongly in brain 2%/2 mm, lung 3%/3 mm and lung 1%/1 mm, as well as moderately in brain 3%/1 mm.

Table 6. *Paired Sample Wilcoxon Signed Ranks test results and Spearman's correlations for gamma analysis threshold comparisons for portal dosimetry with AAA-algorithm*

		Brain		Lung	
		Wilcoxon Signed Ranks Test (5%AAA vs. 60%AAA) (Sig.)	**Spearman's Rho (5%AAA vs. 60%AAA) (Coef./Sig.)**	**Wilcoxon Signed Ranks Test (5%AAA vs. 60%AAA) (Sig.)**	**Spearman's Rho (5%AAA vs. 60%AAA) (Coef./Sig.)**
3%/3mm	6FFF	0.000	0.910/0.000	0.015	0.872/0.000
2%/2mm	6FFF	0.001	0.801/0.000	0.000	0.954/0.000
1%/1mm	6FFF	0.001	0.224/0.262	0.001	0.776/0.000
3%/1mm	6FFF	0.008	0.616/0.001	0.000	0.952/0.000

5.1.3 Comparison of PDIP and AAA algorithms in portal dosimetry

Results and statistics applied by portal dosimetry with PDIP and AAA -algorithms for brain and lung tumors are presented in the following paragraphs.

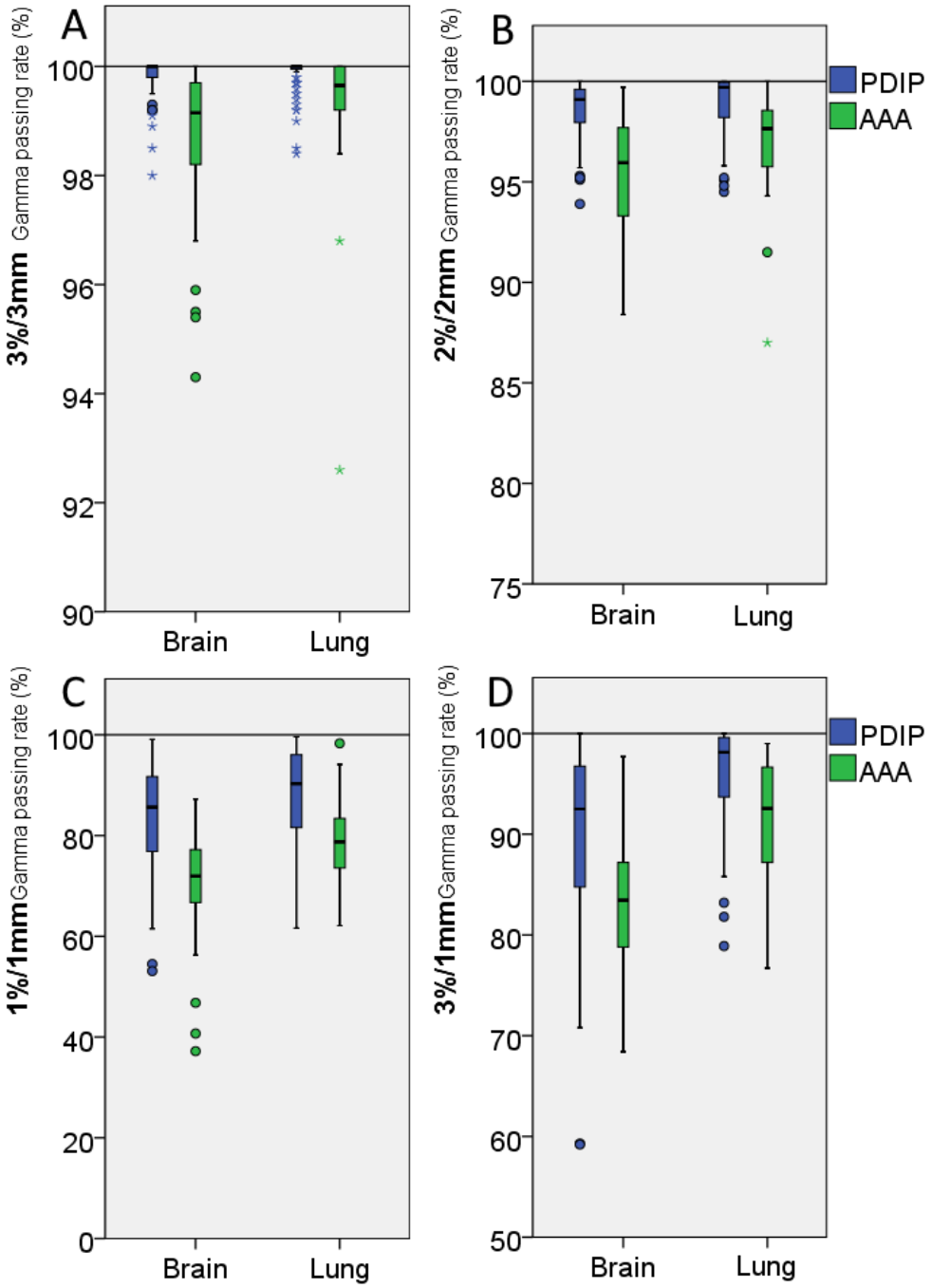

Figure 13. *Box plot –distributions of gamma passing rates for portal dosimetry measurements with PDIP and AAA -algorithms for brain and lung tumors with gamma criteria of 3%/3 mm (A), 2%/2 mm (B),1%/1 mm (C) and 3%/1 mm (D).*

Figure 13. presents the box plot distributions of gamma passing rates for portal dosimetry measurements with PDIP and AAA -algorithms for categories of brain and lung tumors with gamma criteria of 3%/3 mm, 2%/2 mm, 1%/1 mm and 3%/1 mm. According to the visual inspection of the distributions, the portal dosimetry algorithm has a noticeable effect on gamma passing rates with all gamma criteria. The gamma passing rates seem to be higher with PDIP algorithm than with AAA algorithm.

Visual observations about the effect of algorithm can be supported by the Independent-Samples Mann Whitney U test results revealing significant differences (p = 0.000) for all the gamma criteria between PDIP and AAA algorithms.

Table 7. presents results from Paired Samples Wilcoxon Signed Ranks tests and statistically significant (p > 0.05) Spearman's correlations for gamma passing rates with PDIP and AAA algorithms. The paired sample test results reveal that when comparing pairwise the gamma passing rates with PDIP and AAA algorithms, significant differences occur in all the cases. Spearman's correlations reveal that gamma passing rates with different algorithms correlate strongly in brain 60% 2%/2 mm and 3%/1 mm, as well as in lung 5% 2%/2 mm, 5% 1%/1 mm and 5% 3%/1 mm. The gamma passing rates with different algorithms correlate moderately in brain 3%/3 mm, 5% 2%/2 mm and 5% 1%/1 mm, as well as in lung 60% 1%/1 mm and 60% 3%/1 mm.

Table 7. *Paired Sample Wilcoxon Signed Ranks test results and statistically significant (p > 0.05) Spearman's correlations for portal dosimetry algorithm comparison (PDIP vs. AAA) in categories of brain and lung tumors.*

			Brain		**Lung**	
			Wilcoxon Signed Ranks Test (Sig.)	**Spearman's Rho (Coef./Sig.)**	**Wilcoxon Signed Ranks Test (Sig.)**	**Spearman's Rho (Coef./Sig.)**
3%/3mm	6FFF	5 %	0.000	0.509/0.000	0.000	
		60 %	0.000	0.584/0.001	0.004	
2%/2mm	6FFF	5 %	0.000	0.614/0.001	0.000	0.701/0.000
		60 %	0.000	0.729/0.000	0.000	
1%/1mm	6FFF	5 %	0.000	0.632/0.000	0.000	0.783/0.000
		60 %	0.000		0.000	0.588/0.005
3%/1mm	6FFF	5 %	0.000	0.731/0.000	0.000	0.898/0.000
		60 %	0.000	0.732/0.000	0.000	0.636/0.002

5.1.4 I'mRT MatriXX Evolution

Results and statistics applied by array detector I'mRT MatriXX Evolution for brain, lung and prostate tumors are presented in the following paragraphs.

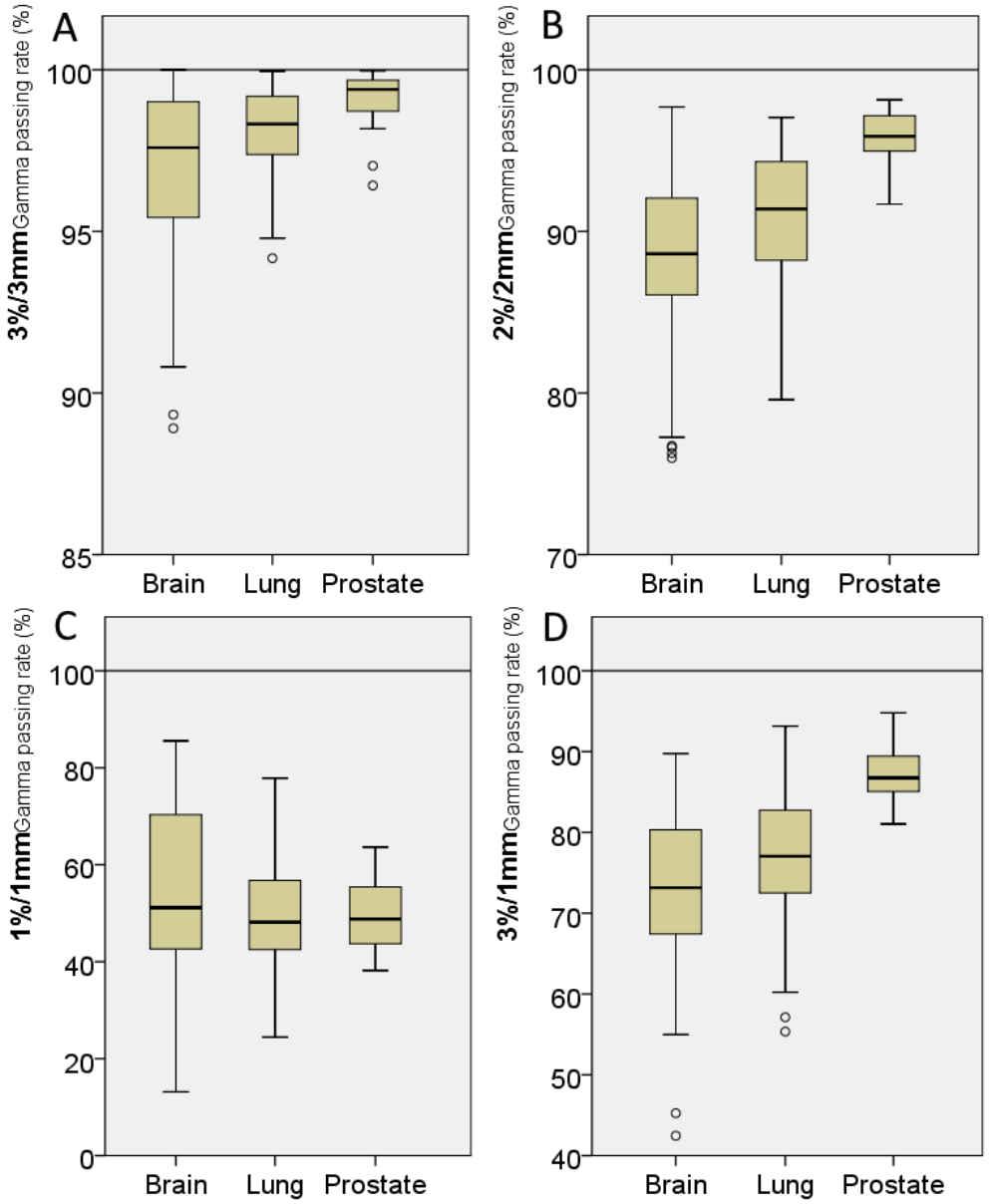

Figure 14. *Box plot –distributions of gamma passing rates for I'mRT MatriXX Evolution measurements. Distributions are presented for brain, lung and prostate tumors with gamma criteria of 3%/3 mm (A), 2%/2 mm (B),1%/1 mm (C) and 3%/1 mm (D).*

Figure 14. presents the box plot distributions of gamma passing rates with gamma criteria of 3%/3 mm, 2%/2 mm, 1%/1 mm and 3%/1 mm for categories of brain, lung and prostate tumors. According to the visual inspection of the distributions, the mean size of the target (brain 5.4 ± 4.3 cm^3, lung 25.3 ± 18.6 cm^3, prostate 84.8 ± 18.1 cm^3) seems to have an predictable effect on gamma passing rates. In case of gamma criteria of 3%/3

mm, 2%/2 mm and 3%/1 mm, the median gamma passing rates increase and the deviations decrease, as the mean target size increases. In case of gamma criteria of 1%/1 mm, the deviation decreases, as the mean target size increases, but no significant effect on median gamma passing rates can be seen.

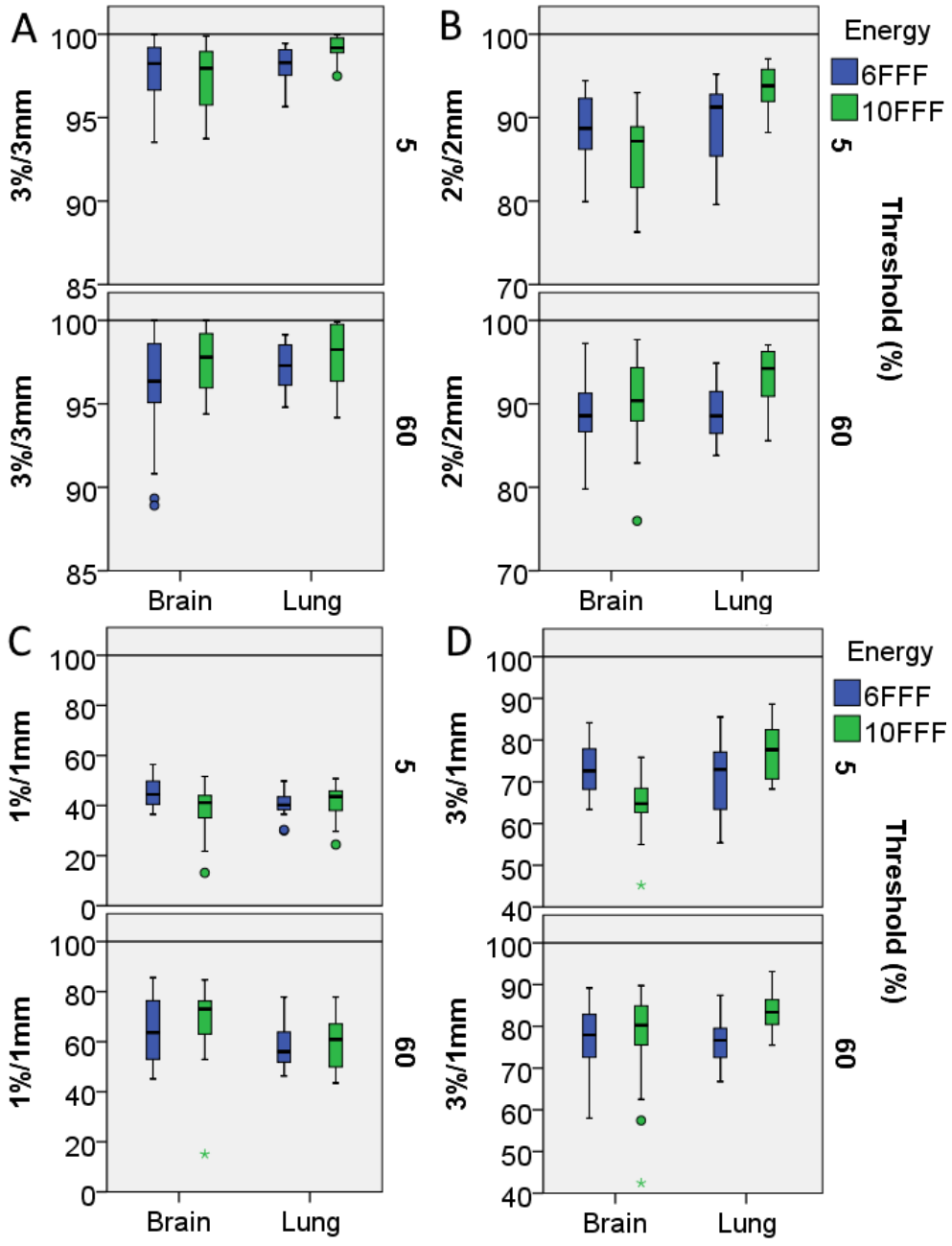

Figure 15. *Box plot –distributions representing the effects of energy (6 FFF and 10 FFF) and threshold (5% and 60%) to gamma passing rates of I'mRT MatriXX Evolution -measurements. Distributions are presented for brain and lung tumors with gamma criteria of 3%/3 mm (A), 2%/2 mm (B),1%/1 mm (C) and 3%/1 mm (D).*

Figure 15. presents more detailed distributions of I'mRT MatriXX Evolution gamma analysis results with gamma analysis thresholds of 5% and 60%, and energies of 6 FFF and

10 FFF. According to the visual inspection of the distributions, the gamma analysis results for 10 FFF beams result in lower gamma passing rates and increased deviations in comparison with 6 FFF for brain tumors. In case of lung tumors, the gamma analysis results for 6 FFF beams result in lower gamma passing rates compared to the 10 FFF.

The threshold of 60% results in higher gamma passing rates and increased deviations compared to the threshold of 5%.

Table 8. presents the descriptive statistics (mean, SD) and Independent-Samples Kruskal-Wallis Test results for brain, lung and prostate tumors. Visual observations can be supported by the descriptive statistics. Independent-Samples Kruskal-Wallis tests reveal that gamma passing rates with 6 FFF (brain vs. lung) do not differ significantly, but in case of 10 FFF (brain, lung, prostate), significant differences occur between target site groups.

Table 8. *Descriptives and Independent-Samples Kruskal-Wallis test results for I'mRT MatriXX Evolution measurement results in categories of brain, lung and prostate tumors.*

	Energy		Brain Mean ± SD	Lung Mean ± SD	Prostate Mean ± SD	Independent-Samples Kruskal-Wallis Test
PTV volume (cm3)	6FFF		6.08±4.28	23.22±18.48		0.000
	10FFF		4.18±3.70	28.18±17.83	84.80±17.56	0.000
MU/Gy	6FFF		267.4±50.7	339.9±82.0		0.002
	10FFF		253.53±16.74	296.15±40.59	303.79±18.29	0.000
		Threshold				
3%/3mm	6FFF	5 %	97.60±1.90	98.23±0.96		0.400
		60 %	96.25±3.00	97.19±1.42		0.383
	10FFF	5 %	97.40±1.90	99.10±0.83	99.48±0.38	0.000
		60 %	97.49±1.89	98.06±1.77	98.84±0.93	0.057
2%/2mm	6FFF	5 %	88.86±4.18	89.19±4.61		0.678
		60 %	88.92±4.47	88.82±3.37		0.876
	10FFF	5 %	85.26±5.25	93.49±2.64	96.25±1.22	0.000
		60 %	90.45±5.04	92.95±3.82	95.22±1.93	0.003
1%/1mm	6FFF	5 %	45.05±6.05	40.53±4.78		0.020
		60 %	64.59±12.63	58.02±8.81		0.090
	10FFF	5 %	39.26±8.76	42.02±6.95	44.56±4.86	0.141
		60 %	68.51±14.84	59.65±10.46	54.83±4.66	0.000
3%/1mm	6FFF	5 %	73.09±5.84	71.46±8.42		0.625
		60 %	77.04±7.53	76.56±5.23		0.633
	10FFF	5 %	64.65±6.16	77.73±6.52	85.44±2.93	0.000
		60 %	77.66±11.10	83.68±4.94	88.60±3.00	0.000

Independent-Samples Kruskal-Wallis Test null hypothesis:
The distribution is the same across categories of Brain/Lung/Prostate.

Table 9. presents Independent Samples Mann-Whitney U test results and correlations from energy comparison of treatment plans executed with 6 FFF or 10 FFF beams. Independent-Samples Mann-Whitney U Test reveals that brain tumors do not show energy dependency ($p > 0.05$), but lung tumors show significant energy dependency for 3%/3 mm, 2%/2 mm and 3%/1 mm. Spearman's correlations reveal that energy do not show correlation for brain tumors, but lung tumors exhibit a moderate correlation with gamma passing criteria 3%/3 mm, 2%/2 mm and 3%/1 mm.

Table 9. *Independent Samples Kruskal-Wallis test results and correlations for I'mRT MatriXX Evolution measurements in categories of 6 FFF and 10 FFF*

	Brain		**Lung**	
	Independent-Samples Mann-Whitney U Test (Sig.)	**Correlations with *energy*: Spearman's Rho (Coef./Sig.)**	**Independent-Samples Mann-Whitney U Test (Sig.)**	**Correlations with *energy*: Spearman's Rho (Coef./Sig.)**
3%/3mm	0.536	0.062/0.539	0.001	0.370/0.001
2%/2mm	0.538	-0.062/0.541	0.000	0.511/0.000
1%/1mm	0.619	-0.050/0.621	0.541	0.070/0.544
3%/1mm	0.058	-0.190/0.058	0.000	0.433/0.000

Independent-Samples Mann-Whitney U Test Null Hypothesis:
The distribution is the same across categories of 6FFF/10FFF.

Table 10. presents results from Paired Sample Wilcoxon Signed Ranks tests and Spearman's correlations for 5% and 60% gamma analysis thresholds. The paired sample test results reveal that when comparing the results with 5% threshold and 60% threshold, significant differences occur in all other cases except 10 FFF 3%/3 mm for brain tumors, 6 FFF 1%/1 mm for lung tumors and 6 FFF 2%/2 mm for brain and lung tumors. Spearman's correlations reveal that gamma passing rates with different thresholds correlate very strongly in brain 6 FFF 3%/3 mm and lung 6 FFF 3%/3 mm. The gamma passing rates with different thresholds correlate strongly in brain 10 FFF 3%/3 mm, 6 FFF 2%/2 mm, 10 FFF 2%/2 mm, 6 FFF 1%/1 mm and 10 FFF 1%/1 mm, as well as in lung 10FFF 3%/3mm. The gamma passing rates with different thresholds correlate moderately in lung 6 FFF 2%/2 mm, 10 FFF 1%/1 mm and 6 FFF 3%/1 mm.

Table 10. *Paired sample Wilcoxon Signed Ranks test results and Spearman's correlations for I'mRT MatriXX Evolution in categories of brain, lung and prostate tumors.*

		Brain		Lung		Prostate	
		Wilcoxon Signed Ranks Test (5%MATRIX vs. 60%MATRIX) (Sig.)	**Spearman's Rho (5%MATRIX vs. 60%MATRIX) (Coef./Sig.)**	**Wilcoxon Signed Ranks Test (5%MATRIX vs. 60%MATRIX) (Sig.)**	**Spearman's Rho (5%MATRIX vs. 60%MATRIX) (Coef./Sig.)**	**Wilcoxon Signed Ranks Test (5%MATRIX vs. 60%MATRIX) (Sig.)**	**Spearman's Rho (5%MATRIX vs. 60%MATRIX) (Coef./Sig.)**
3%/3mm	6FFF	0.000	0.905/0.000	0.000	0.742/0.000		
	10FFF	0.939	0.801/0.000	0.000	0.909/0.000	0.000	0.971/0.000
2%/2mm	6FFF	0.801	0.811/0.000	0.509	0.649/0.001		
	10FFF	0.000	0.701/0.000	0.943	0.536/0.022	0.000	0.967/0.000
1%/1mm	6FFF	0.000	0.897/0.000	0.000	0.310/0.171		
	10FFF	0.000	0.713/0.000	0.000	0.618/0.006	0.000	0.808/0.000
3%/1mm	6FFF	0.008	0.465/0.017	0.012	0.455/0.038		
	10FFF	0.001	0.448/0.032	0.005	0.405/0.095	0.001	0.631/0.005

5.1.5 Comparison of Portal dosimetry and I'mRT MatriXX Evolution

Results and statistics applied by portal dosimetry with PDIP and AAA-algorithms as well as array detector I'mRT MatriXX Evolution for brain, lung and prostate tumors are presented in the following paragraphs.

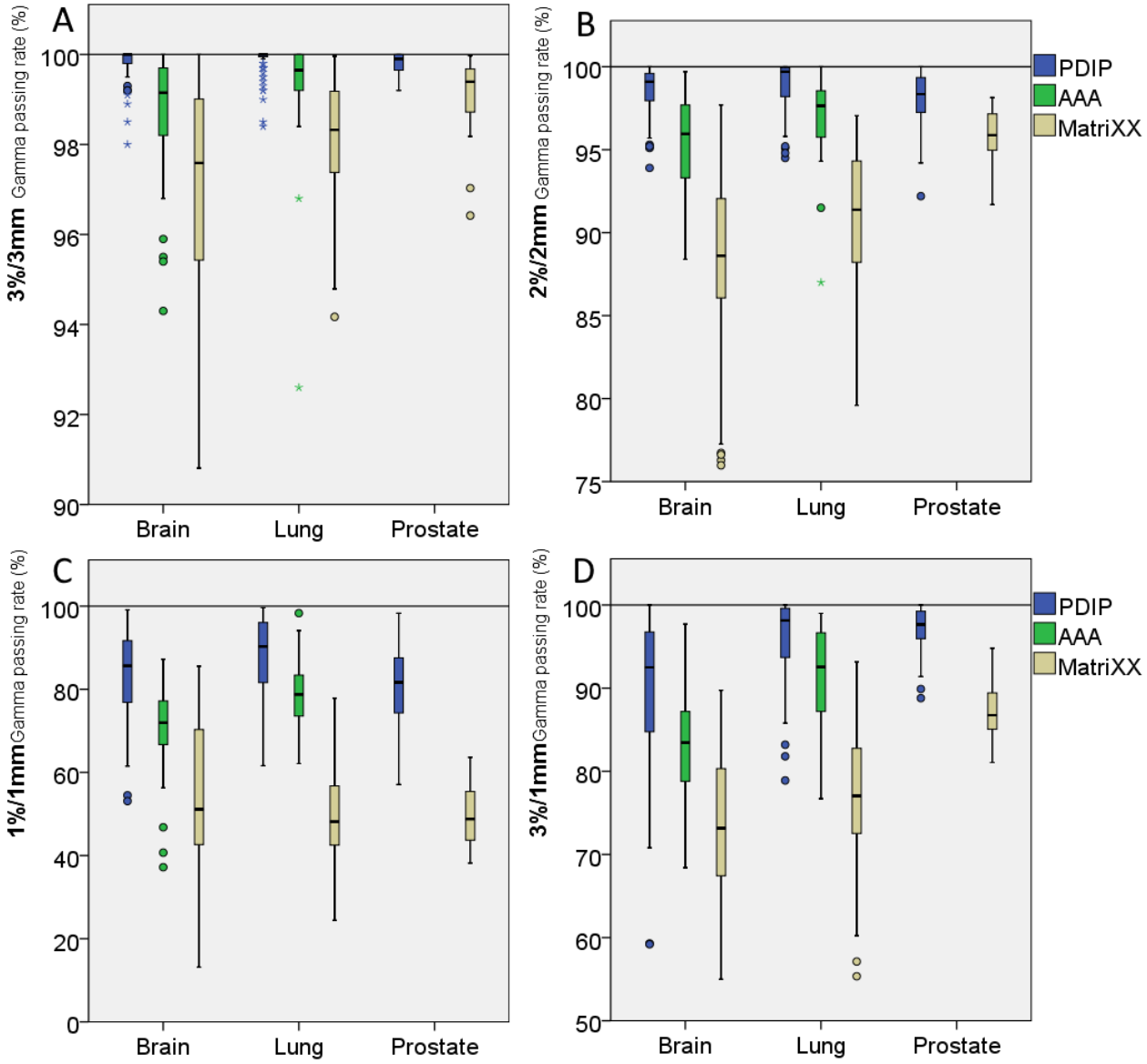

Figure 16. *Box plot –distributions of gamma passing rates for portal dosimetry measurements with PDIP and AAA –algorithms and I'mRT MatriXX Evolution measurement for brain, lung and prostate tumors with gamma criteria of 3%/3 mm (A), 2%/2 mm (B),1%/1 mm (C) and 3%/1 mm (D).*

Figure 16. presents the box plot -distributions of gamma passing rates with gamma criteria of 3%/3 mm, 2%/2 mm, 1%/1 mm and 3%/1 mm for categories of brain, lung and prostate tumors. According to the visual inspection of the distributions, the measurement

method (portal dosimetry with PDIP or AAA algorithms, or I'mRT MatriXX Evolution) has a significant visual effect on gamma passing rates with the all gamma criteria. The gamma passing rates decrease and the deviations increase from PDIP to AAA and AAA to I'mRT MatriXX Evolution.

Independent-Samples Kruskal-Wallis Tests for brain, lung and prostate tumors in categories of PDIP/AAA/I'mRT MatriXX Evolution reveal that gamma passing rates differ significantly ($p = 0.000$) for all the target sites between categories PDIP, AAA and I'mRT MatriXX Evolution.

Table 11. presents statistically significant results from Paired Sample Wilcoxon Signed Ranks tests and statistically significant Spearman's correlations for 6 FFF and 10 FFF energies, and 5% and 60% gamma analysis thresholds. Paired Sample Wilcoxon Signed Rank tests reveal that gamma passing rates with PDIP differ significantly from gamma passing rates with I'mRT MatriXX Evolution and the gamma passing rates with AAA differ significantly from the gamma passing rates with I'mRT MatriXX Evolution.

I'mRT MatriXX Evolution results do not correlate with PDIP or AAA (except moderate correlations in PDIP 10 FFF 3%/3 mm, 10 FFF 5% 2%/2 mm, 10 FFF 5% 1%/1 mm and 10 FFF 60% 3%/1 mm, as well as in AAA 60% 1%/1 mm).

Table 11. *Statistically significant results from Paired Sample Wilcoxon Signed Ranks tests and statistically significant Spearman's correlations for 6FFF and 10FFF energies, and 5% and 60% gamma analysis thresholds.*

				Brain		Lung		Prostate	
				Wilcoxon Signed Ranks Test (Sig.)	Spearman's Rho (Coef./Sig.)	Wilcoxon Signed Ranks Test (Sig.)	Spearman's Rho (Coef./Sig.)	Wilcoxon Signed Ranks Test (Sig.)	Spearman's Rho (Coef./Sig.)
PDIP vs. I'mRT MatriXX Evolution	3%/3mm	6FFF	5 %	0.000		0.000			
			60 %	0.000		0.000			
		10FFF	5 %	0.000		0.000	0.556/0.017	0.004	
			60 %	0.000		0.000	0.490/0.039	0.001	
	2%/2mm	6FFF	5 %	0.000		0.000			
			60 %	0.000		0.000			
		10FFF	5 %	0.000		0.000	0.481/0.043	0.000	
			60 %	0.000		0.000		0.005	
	1%/1mm	6FFF	5 %	0.000		0.000			
			60 %	0.000		0.000			
		10FFF	5 %	0.000		0.000	0.494/0.037	0.000	
			60 %	0.287		0.000		0.000	
	3%/1mm	6FFF	5 %	0.000		0.000			
			60 %	0.000		0.000			
		10FFF	5 %	0.000		0.000		0.000	
			60 %	0.715		0.001	0.606/0.008	0.000	
AAA vs. I'mRT MatriXX Evolution	3%/3mm	6FFF	5 %	0.001		0.000			
			60 %	0.004		0.001			
	2%/2mm	6FFF	5 %	0.000		0.000			
			60 %	0.000		0.000			
	1%/1mm	6FFF	5 %	0.000		0.000			
			60 %	0.000	0.493/0.009	0.000			
	3%/1mm	6FFF	5 %	0.000		0.000			
			60 %	0.000		0.000			

Table 12. presents comparison of gamma passing rate pass/fail threshold result of > 95% (x), 95% > γ > 90% (o), 90% > γ (-). PDIP results of 3%/3 mm and 2%/2 mm fulfil the gamma pass threshold of > 95%. PDIP results of 3%/1mm fulfil the gamma pass threshold of > 90%, except in case of brain 10FFF. AAA results of 3%/3 mm fulfil the gamma pass threshold of > 95% and results of 2%/2 mm fulfil the gamma pass threshold of > 90%. I'mRT MatriXX Evolution results of 3%/3 mm fulfil the gamma pass threshold of > 95%.

Table 12. *Comparison of gamma passing rate pass/fail result of >95% (x), 95%>γ>90% (o), 90%>γ (-).*

			PDIP			AAA		MatriXX		
			Brain	**Lung**	**Prostate**	**Brain**	**Lung**	**Brain**	**Lung**	**Prostate**
3%/3mm	6FFF	5 %	x	x		x	x	x	x	
		60 %	x	x		x	x	x	x	
	10FFF	5 %	x	x	x			x	x	x
		60 %	x	x	x			x	x	x
2%/2mm	6FFF	5 %	x	x		x	x	–	–	
		60 %	x	x		o	x	–	–	
	10FFF	5 %	x	x	x			–	o	x
		60 %	x	x	x			o	o	x
1%/1mm	6FFF	5 %	o	x		–	–	–	–	
		60 %	–	o		–	–	–	–	
	10FFF	5 %	–	–	–			–	–	–
		60 %	–	–	–			–	–	–
3%/1mm	6FFF	5 %	x	x		–	o	–	–	
		60 %	o	x		–	–	–	–	
	10FFF	5 %	–	o	x			–	–	–
		60 %	–	o	x			–	–	–

5.2 Average percentual dose difference

Average percentual dose difference results and statistics applied by portal dosimetry with PDIP and AAA-algorithms for brain, lung and prostate tumors are presented in the following paragraphs.

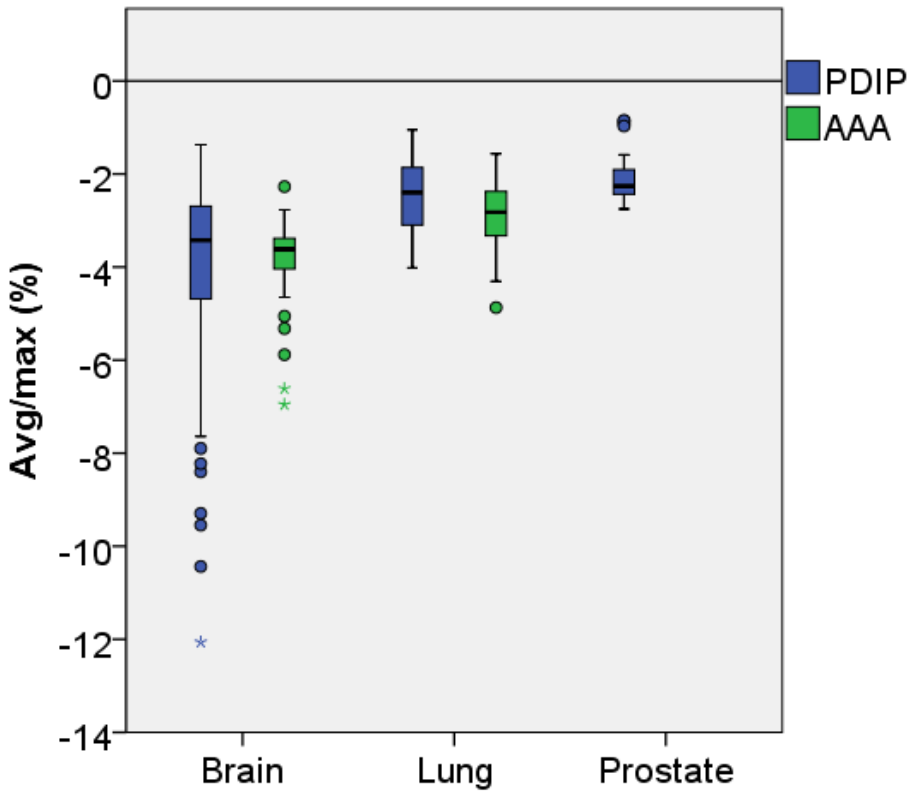

Figure 17. *The box plot distributions of average percentual dose differences (Avg/Max) between measured and predicted doses for portal dosimetry with PDIP and AAA –algorithms in categories of brain, lung and prostate tumors.*

Figure 17. presents the box plot distributions of average percentual dose differences between measured and predicted doses for portal dosimetry with PDIP and AAA –algorithms. According to the visual inspection of the distributions, the mean size of the target (brain 5.4 ± 4.3 cm^3, lung 25.3 ± 18.6 cm^3, prostate 84.8 ± 18.1 cm^3) seems to have an effect on average percentual dose difference on both portal dosimetry algorithms. The average percentual dose difference decreases. In case of PDIP –algorithm, the deviation decreases, as the mean target size increases. Table 13. presents the descriptive statistics (mean, SD) and Independent-Samples Kruskal-Wallis Test results for brain, lung and

prostate targets. Visual observations can be supported by the descriptive statistics. Independent-Samples Kruskal-Wallis tests reveal that the average percentual dose differences with PDIP or AAA-algorithms differ significantly between target site groups.

Table 13. *Decsriptives and Independent samples Kruskal-Wallis test results in categories Brain/Lung/Prostate*

		Energy	Threshold	Brain Mean ± SD	Lung Mean ± SD	Prostate Mean ± SD	Independent-Samples Kruskal-Wallis Test
Avg/Max	PDIP	6FFF	5 %	-2.68±0.43	-1.96±0.53		0.000
			60 %	-3.27±1.25	-2.07±0.67		0.000
	AAA		5 %	-3.55±0.34	-3.07±0.53		0.001
			60 %	-4.07±1.09	-2.77±0.87		0.000
	PDIP	10FFF	5 %	-4.08±0.54	-2.99±0.43	-2.25±0.52	0.000
			60 %	-6.51±2.50	-3.10±0.69	-1.93±0.44	0.000

Independent-Samples Kruskal-Wallis Test null hypothesis:
The distribution is the same across categories of Brain/Lung/Prostate.

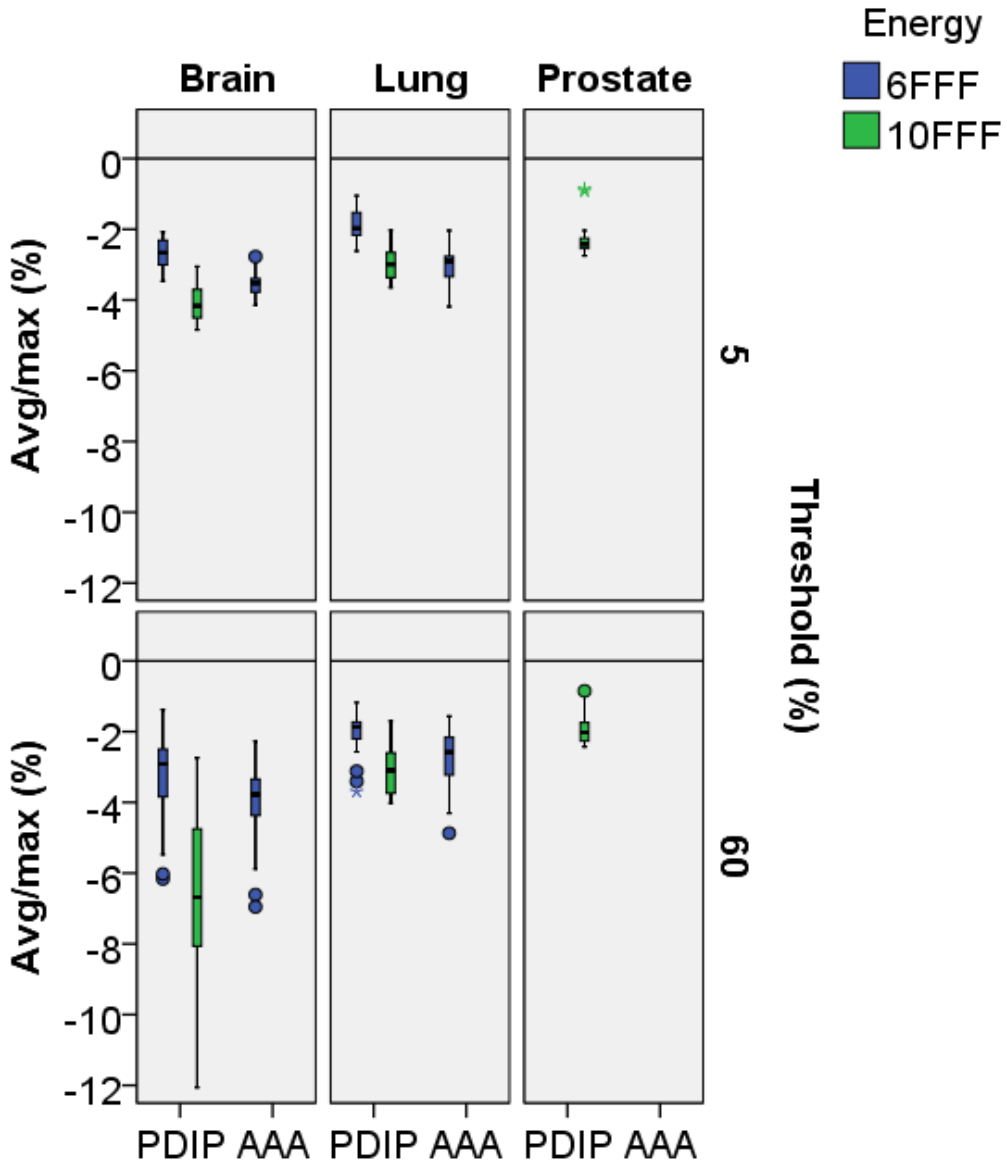

Figure 18. *The box plot -distributions of average percentual dose difference (Avg/Max) for gamma analysis thresholds of 5% and 60% for PDIP and AAA –algorithms and 6 FFF and 10 FFF energies*

Figure 18. presents the box plot -distributions of average percentual dose difference for gamma analysis thresholds of 5% and 60% for PDIP and AAA –algorithms and 6 FFF and 10 FFF energies. According to the visual inspection, the average percentual dose difference increases and the deviation increases as the the energy increases from 6FFF to 10FFF. The effect of energy can be seen in both tumor sites (brain and lung), but is more pronounced in brain tumors. The average percentual dose difference increases and the deviation increases with the threshold of 60% in comparison with the threshold of 5%.

Table 14. presents the independent samples tests, paired samples tests and correlations for average percentual dose difference. Independent-Samples Mann-Whitney U Test reveals that average percentual dose difference in brain metastases and lung tumors show significant energy dependency. The paired sample test results reveal that when comparing the results with 5% threshold and 60% threshold, significant differences occur in PDIP-results for brain, AAA-results for lung and PDIP-results for prostate. Spearman's correlations reveal that the average percentual dose difference values correlate very strongly in lung PDIP 10FFF. The average percentual dose difference values correlate strongly in brain PDIP 6FFF, and in lung PDIP 6FFF, lung AAA 6FFF, as well as in prostate PDIP. The average percentual dose difference values correlate moderately in brain PDIP 10FFF.

Table 14. *Independent samples tests, paired samples tests and correlations for average percentual dose difference (Avg/Max)*

		Brain		**Lung**		**Prostate**
		Independent-Samples Kruskal-Wallis Test (Sig.) Null Hypothesis: The distribution is the same across categories of PDIP/AAA				
Avg/Max		0.000		0.000		
		Independent-Samples Mann-Whitney U Test (Sig.) Null Hypothesis: The distribution is the same across categories of PDIP 6FFF/10FFF.				
Avg/Max	6FFF 10FFF	0.000		0.000		
		Paired Samples: Wilcoxon Signed Ranks Test (Sig.)				
		5%PDIP vs. 60%PDIP	**5%AAA vs. 60%AAA**	**5%PDIP vs. 60%PDIP**	**5%AAA vs. 60%AAA**	**5%PDIP vs. 60%PDIP**
Avg/Max	6FFF	0.002	0.074	0.498	0.015	
	10FFF	0.000		0.286		0.000
		Correlations: Spearman's Rho (Coef./Sig.)				
		5%PDIP vs. 60%PDIP	**5%AAA vs. 60%AAA**	**5%PDIP vs. 60%PDIP**	**5%AAA vs. 60%AAA**	**5%PDIP vs. 60%PDIP**
Avg/Max	6FFF	0.796/0.000	0.125/0.534	0.788/0.000	0.826/0.000	
	10FFF	0.522/0.011		0.901/0.000		0.858/0.000

6. DISCUSSION

The utilization of VMAT-technique in stereotactic treatments has rapidly increased. Treatments executed with VMAT-technique are comprised of small fields and even smaller subfields. The small field size induces different kinds of dosimetric challenges. Dosimetric challenges include detector size, steep dose gradient, loss of charged particle equilibrium, volume averaging effect and partial occlusion of the primary photon source by the collimating devices. In addition, small field size induces also dosimetric challenges due to small MLC apertures, high transmission, DLG and tongue and groove effects, as well as their effects on dose calculation. The small target volumes challenge the different measurement methods in varying amount.

IMRT/VMAT techniques have enabled higher conformal radiation doses in the tumor, compared to the conventional techniques, and sparing of normal tissues surrounding the tumor site. These advanced radiation therapy techniques have increased the accuracy requirements for dose delivery. With stereotactic high dose treatments, the importance of the quality assurance of treatment plans is highlighted and the dosimetric performances of measurement devices need to be carefully assessed.

The quality assurance of treatment plans is an important part of execution of stereotactic treatments. In daily practice, the effortlessness and speed of these procedures are important factors when selecting the appropriate measurement method.

Previously the film measurements have been considered as the gold standard for quality assurance of treatment plans, as it is the oldest method and has an extremely high spatial resolution. However, the radiochromic film has significant disadvantages. The calibration curve is determined by irradiating pieces of the film with known different doses, separately for each experiment. The calibration film and the measurement film are irradiated on the same day, and the scanning of those is carried out on the same day and in the same orientation respect to the original orientation, but a waiting period between the irradiation and scanning is required to guarantee the stabilization of the film darkening. The storage conditions of the films and time between the irradiation and scanning are required to be constant. The radiochromic films exhibit significant variation in optical density when the light source is linearly polarized, so the orientation of the film in the scanner is crucial. In conclusion, for practical purposes, reliable film dosimetry protocols are too laborious to establish.

For measurements using sparse array detectors, interpolation to a finer resolution and resampling of the dose distribution to the configuration of the detector array will be required. These processes can introduce uncertainties for the measurement results.

The advances of the portal dosimetry are fast image acquisition, high resolution and digital format. However, the dose is modelled in the ideal portal detector plate, but the response might change in time and might be individual for each detector plate. The PDIP calculation can be re-configured time by time to take into account the change in the response. The AAA calculation model do not take into account these variations and the significance of this effect is difficult to estimate.

A shortage of this thesis is fixed positions of both measurement devices in the gantry geometry. The effects of couch rotations cannot be measured and true 3D dose distribution stays unknown. Statistical tests evaluate the stochastic errors of the methods, but they cannot evaluate the systematic errors of the methods. The amount of data is quite small in this thesis, so the results include uncertainty in some amount. In case of small stereotactic targets, the exact placement of measurement device in the radiation field might cause systematic errors in the results, especially in case of detector arrays.

With all the measurement methods, the “truth” stays unclear, as all the different measurement methods have limitations. The importance of optimization of DLG has been reported in literature (18, 19, 38-40). Kielar et al. (18) investigated the rounded leaf effect on the HD120™ MLC of Varian TrueBeam™ STx linac. DLG value was determined using MLC-defined field sizes and moving gap test. After that they optimized the DLG-value in the Eclipse treatment planning system to achieve less than 1% difference between measured and calculated dose. The optimized DLG value was tested on treatment plans for all energies and treatment modalities available on the linac with ionization chamber and film measurements. They found that the DLG parameter found during the initial MLC testing did not match the leaf gap modelling parameter that provided the most accurate dose delivery in clinical treatment plans.

The tuning of the DLG could make the measurement distributions to agree well with the predicted distribution, but the exact truth about the ability of the treatment machine to deliver the given treatment plan remains still a bit uncertain. The tuning of the DLG affects both the measured dose distribution and the predicted dose distribution, so the effects might not be straightforward.

The aim of this study was to quantitatively compare measurement methods for QA of stereotactic treatment plans. Portal dosimetry measurements with PDIP and AAA -algorithms were compared with array detector measurements with I’mRT MatriXX Evolution.

The both measurement devices were dose calibrated before measurements according to the manufacturer recommended protocols. Principled errors related to the absolute dose calibration should not occur, but target size dependent errors might occur. It is of outmost importance to know the differences between different measurement methods. This thesis gives quantitative information for QA of stereotactic treatment plans from portal dosimetry with PDIP and AAA dose calculation algorithms, and I'mRT MatriXX Evolution array detector with constant study material.

In this thesis, the PDIP results showed that the target volume has a weak effect on gamma passing rates, being most pronounced on gamma criterion 3%/1mm. Gamma passing rates increase as the target volume increases.

PDIP results also showed an energy dependency, especially with tighter gamma criteria. PDIP measurements result in higher gamma passing rates for treatment plans with 6 FFF beam than 10 FFF beams.

Xu et al. (41) investigated the dose rate response characteristics of the Varian aS1200-detector. The IMRT dose rate study for gamma index analysis showed that the gamma index agreement decreased when the dose rate increased. For 6 FFF fields, the gamma index agreement decreased from 100% to 97.8% with dose rate increasing from 400 to 1400 MU/min. For 10 FFF fields, the gamma index agreement decreased from 99.9% to 91.5% whit dose rate increasing from 400 to 2400 MU/min. The open field measurement showed only about 1% increase in central portal dose from 400 to 2400 MU/min. Based on these results, Xu et al. discussed that the decrease in the gamma agreement index is mainly due to the challenges caused by the high dose rate to the MLC motion. (41)

The findings by Xu et al. might explain the energy dependency of our PDIP results. On the other hand, their discussion about the reasons for the energy dependency (challenges of the MLC with high dose rate) does not explain why PDIP results and I'mRT MatriXX Evolution results differ. The backscatter might affect the results with 10 FFF, although the aS1200 detector has an improved backscatter shielding.

Energy comparison (6 FFF vs. 10 FFF) of average percentual dose difference results with PDIP showed that the energy dependency occurs on both tumor groups (brain and lung) but is more pronounced on brain tumors. The average percentual dose difference increases and the deviation increases as the energy increases from 6 FFF to 10 FFF.

Average percentual dose difference results showed that the mean size of the target has an effect on the average percentual dose difference results. The average percentual dose difference decreases and the deviation decreases, as the mean target size increases.

Covington et al. (7) assessed the feasibility of single target 10 FFF SRS QA with portal dosimetry, delivered with Varian Edge linear accelerator equipped with HDMLC and aS1200 portal dose imager. The average measured portal image to PDIP predicted image dose was 0.992 ± 0.02, indicating that the measured dose was smaller than the predicted dose. The average film to treatment planning system dose in the high dose region was 1.026 ± 0.01. When they compared the mean dose in the film with the mean dose in the portal image, they found target size dependence: with target diameters greater than 15 mm, the ratio was 1.03, with target diameters of less than 15 mm the ratio was 1.05, with the smallest diameters, the ratio was 1.08. They also studied the dose rate effect on portal imaging results and the lowest dose rate of 400 MU/min resulted in the greatest agreement with the predicted image and the clinically used dose rate of 2400 MU/min showed an increased difference at smaller field sizes. They conclude that the portal dosimetry measurement results were target size dependent and could deviate up to 8% from film measurements for the smallest target. (7)

The findings by Covington et al. support the findings of this study about the fact that the measured doses are smaller than the predicted doses, and are target size dependent.

I'mRT MatriXX Evolution results showed that the target volume has a strong effect on gamma passing rates. Gamma passing rates increase and deviations decrease as the target volume increases. I'mRT MatriXX Evolution results also showed an energy dependency for lung tumors, especially with tighter gamma criteria. I'mRT MatriXX Evolution lung tumor results with higher gamma passing rates for treatment plans with 10 FFF beam than 6 FFF beams. On the other hand, brain tumors do not show energy dependency. The sparse spatial resolution of I'mRT MatriXX Evolution array detector probably explains the target volume dependency. The energy dependency might result from the backscatter, sensitivity of the array detector to different energies or the uncertainties in the dose calculations. Mean energy of the 6 FFF beam might be too low for the array to work properly.

Chung et al. (6) compared the performance of different commercial QA systems for pretreatment QA of SBRT treatment plans (lung, spine and prostate tumors) with VMAT and FFF-beams. QA systems tested were a film, I'mRT MatriXX and MapCHECK. Gamma evaluation with gamma criteria of 2%/2 mm and 3%/3 mm was analyzed. The highest gamma passing rates were obtained with MapCHECK and lowest gamma passing rates were obtained with film. Gamma passing rates with I'mRT MatriXX were 93.6% for gamma criterion 2%/2 mm and 98.2% for gamma criterion of 3%/3 mm. Gamma passing rates with I'mRT MatriXX for 6 FFF were 93.8% ± 1.8% for 2%/2 mm and 98.0% ± 1.3% for 3%/3 mm. Gamma passing rates for 10 FFF were 93.4% ± 1.7% for 2%/2 mm and

98.3% ± 1.5% for 3%/3 mm. Gamma passing rates agree well with gamma passing rates obtained in this these with I'mRT MatriXX Evolution for treatment plans of lung and prostate tumors, but results in this thesis show more pronounced effect of beam energy to gamma passing rates.

Result comparison of PDIP, AAA and I'mRT MatriXX Evolution measurements reveal that the measurement method has a significant effect on gamma passing rates with all gamma criteria. The gamma passing rates decrease and the deviation increase from PDIP to AAA and AAA to I'mRT MatriXX Evolution. PDIP results correlate with AAA results, but I'mRT MatriXX Evolution results do not correlate with PDIP or AAA results. These results can be probably explained by the resolutions of the measurement devices. The comparison of PDIP and AAA –algorithms in portal dosimetry reveals, that the measurements with PDIP-calculations result in higher gamma passing rates than with AAA-calculations. No articles about the comparison of portal dosimetry results with PDIP and AAA algorithms were found in the literature, as the AAA as a portal prediction algorithm is quite new option.

The reliability of the gamma index analysis in detecting clinically significant errors has been questioned in the literature. Nelms et al. (29) investigated the IMRT QA rates and clinically relevant dose errors. They questioned the power of standard acceptance criteria to predict the clinically relevant patient dose errors and the certainty to which abiding the standards mitigates risk of significant error. They introduced the scenarios of "false positive" and "false negative". "False positive" stands for the case in which the beam-by-beam QA results fail to meet criteria, although the clinical impact can be considered negligible. "False negative" stands for the case in which beam-by-beam QA results meet the criteria, but still relevant and actionable patient dose errors occur. They conclude that in both scenarios, the magnitude and location of the errors may prove to be more critical than the quantity of the errors described by the passing rates per field and the gamma passing rates are not sensitive to clinically relevant patient dose errors on a per-patient basis. Meeting the Gamma passing rate criteria does not guarantee that clinically acceptable dose errors are within tolerance per patient, neither not meeting gamma passing rates does not imply that clinically relevant dose differences would be significant.

However, the gamma index analysis has been widely accepted method, and it is implemented into most analysis software of commercial measurement devices. The advantage of gamma index tool is that it is an efficient tool in the busy clinical environment. The understanding of the limitations and sensitivity of the gamma index analysis in case of a particular measurement device is important, as the same passing criteria will end up with different results, depending on the particular measurement device. As shown in this

thesis, the same passing criteria do not give the same results for measurements with different measurement devices.

In clinical QA routine, the gamma passing rate is calculated and a pass/fail threshold is set to determine whether the treatment plan pass or fail the quality assurance measurement, i.e. whether the treatment plan is clinically acceptable or not. The gamma criterion of 3%/3 mm is commonly used in the gamma analysis of treatment plans, but might be too loose criterion for stereotactic plans with narrow PTV margins. The gamma criterion of 1%/1 mm is very tight criterion, taking into account the resolution of different measurement methods. The gamma criterion 3%/1mm might be considered appropriate for stereotactic treatment plans, as it gives an opportunity to examine the geometrical accuracy of the dose delivery, allowing 3% variation in the dose level due to the measurement method, treatment planning system and treatment machine based inaccuracies.

A common passing threshold for 3%/3 mm is 95%, meaning that the treatment plan is clinically acceptable, if the gamma passing rate is higher than 95%. With tighter gamma criteria (i.e. 3%/1 mm), looser gamma passing threshold, for example 90% might be more reasonable, depending on the measurement method. On the other hand, for stereotactic treatment plans, high accuracy is required.

The results in passing or failing the gamma pass threshold (table 12.) showed that for portal dosimetry measurements with PDIP algorithm, results with gamma analysis criteria 3%/3 mm and 2%/2 mm pass the gamma pass threshold of 95%. PDIP results with gamma analysis criteria 3%/1 mm pass the gamma pass threshold of 90% in all other cases but 10 FFF brain tumors, i.e. the smallest targets with 10 FFF beams. For portal dosimetry measurements with AAA algorithm, results with gamma analysis criterion 3%/3 mm pass the gamma pass threshold of 95% and results with gamma analysis criterion 2%/2 mm pass the gamma pass threshold of 90%. For I'mRT MatriXX Evolution measurements, results with gamma analysis criterion 3%/3 mm pass the gamma pass threshold of 95% and results with gamma analysis criterion 2%/2 mm pass the gamma pass threshold of 90% for 10 FFF energy, except brain 5%. Results with gamma analysis criterion 2%/2 mm for 6 FFF and tighter gamma criteria fail the both gamma pass thresholds. In conclusion, the portal dosimetry measurements with PDIP and AAA –algorithms, as well as array detector measurement with I'mRT MatriXX give congruent pass/fail results with gamma criteria of 3%/3 mm. The I'mRT MatriXX Evolution array detector is not the most suitable option for stereotactic measurements, mainly due to the sparse spatial resolution, but it can be utilized to separate the unacceptable treatment plans from acceptable ones with coarse gamma criterion of 3%/3mm and pass/fail threshold of 95%. For portal dosimetry measurement with PDIP-algorithm, tighter gamma criteria can be

recommended, for example 3%/1mm with 90% pass/fail threshold. Utilization of portal dosimetry with AAA algorithm needs further studies, as no literature can be found at the moment.

Results from the gamma analysis with different gamma analysis thresholds (5% or 60%) indicate the importance of the careful selection of gamma analysis threshold in the quality assurance protocol. In case of threshold of 60%, only the high dose region is taken into account in the analysis. In case of threshold of 5%, also the low dose region of the distribution is taken into account, but the noise is removed from the analysis.

7. CONCLUSIONS

This thesis gives quantitative information of Varian portal dosimetry and IBA I'mRT MatriXX Evolution –array detector, and how different variables affect the measurement results with these detectors. As a conclusion, the QA results of stereotactic treatment plans are dependent on measurement system, radiation beam energy, target volume, and analysis parameters such as threshold.

Measurement results obtained with different measurement methods cannot be compared directly. Different measurement systems can be used for different treatment plan types. Analysis parameters, such as gamma analysis threshold, gamma analysis criteria and gamma pass/fail threshold are required to be determined in the QA protocol separately to each measurement device, to guarantee the comparability of measurement results.

REFERENCES

[1] Taylor A, Powell MEB. Intensity-modulated radiotherapy--what is it? Cancer imaging : the official publication of the International Cancer Imaging Society. 2004;4(2):68-73.

[2] Benedict SH, Yenice KM, Followill D, Galvin JM, Hinson W, Kavanagh B, et al. Stereotactic body radiation therapy: The report of AAPM Task Group 101. Med Phys. 2010;37(8):4078-101.

[3] Low DA, Moran JM, Dempsey JF, Dong L, Oldham M. Dosimetry tools and techniques for IMRT. Med Phys. 2011;38(3):1313-38.

[4] Low DA, Harms WB, Mutic S, Purdy JA. A technique for the quantitative evaluation of dose distributions. Med Phys. 1998;25(5):656-61.

[5] Varian Medical Systems. Portal Dosimetry Reference Guide. Varian Medical Systems; 2013 Nov.

[6] Chung J, Kang S, Eom K, Song C, Choi K, Suh TS. Comparison of Dosimetric Performance among Commercial Quality Assurance Systems for Verifying Pretreatment Plans of Stereotactic Body Radiotherapy Using Flattening-Filter-Free Beams. J Korean Med Sci. 2016;31(11):1742-8.

[7] Covington EL, Snyder JD, Wu X, Cardan RA, Popple RA. Assessing the feasibility of single target radiosurgery quality assurance with portal dosimetry. J Appl Clin Med Phys. 2019;20(5):135-40.

[8] Lahtinen T, Holsti LR, editors. Kliininen säteilybiologia. Helsinki: Duodecim; 1997.

[9] Khan FM. The Physics of Radiation Therapy. 4th ed. LWW; 2009.

[10] LoSasso T, Chui CS, Ling CC. Physical and dosimetric aspects of a multileaf collimation system used in the dynamic mode for implementing intensity modulated radiotherapy. Med Phys. 1998 Oct;25(10):1919-27.

[11] Budgell G, Brown K, Cashmore J, Duane S, Frame J, Hardy M, et al. IPEM topical report 1: guidance on implementing flattening filter free (FFF) radiotherapy. Phys Med Biol. 2016;61(23):8360-94.

[12] Pardo E, Novais JC, Molina López MY, Maqueda SR. On flattening filter-free portal dosimetry. Journal of Applied Clinical Medical Physics. 2016;17(4):132-45.

[13] Tenhunen M. Sädehoidon fysiikka ja tekniikka. Helsinki: 2007.

[14] Otto K. Volumetric modulated arc therapy: IMRT in a single gantry arc. Med Phys. 2008;35(1):310-7.

[15] Park S, Kim J, Chun M, Ahn H, Park JM. Assessment of the modulation degrees of intensity-modulated radiation therapy plans. Radiation Oncology. 2018;13(1):244.

[16] Varian Medical Systems. Eclipse Photon and Electron Algorithms Reference Guide. Varian Medical Systems; 2015 Mar.

[17] Ulmer W, Harder D. A Triple Gaussian Pencil beam Model for Photon beam Treatment Planning. Zeitschrift für Medizinische Physik. 1995;5(1):25-30.

[18] Kielar KN, Mok E, Hsu A, Wang L, Luxton G. Verification of dosimetric accuracy on the TrueBeam STx: rounded leaf effect of the high definition MLC. Medical physics. 2012 Oct;39(10):6360-71.

[19] Kumaraswamy LK, Schmitt JD, Bailey DW, Xu ZZ, Podgorsak MB. Spatial variation of dosimetric leaf gap and its impact on dose delivery. Med Phys. 2014;41(11):111711.

[20] Yao W, Farr JB. Determining the optimal dosimetric leaf gap setting for rounded leaf-end multileaf collimator systems by simple test fields. Journal of Applied Clinical Medical Physics. 2015;16(4):65-77.

[21] Miri N, Keller P, Zwan BJ, Greer P. EPID-based dosimetry to verify IMRT planar dose distribution for the aS1200 EPID and FFF beams. Journal of Applied Clinical Medical Physics. 2016;17(6):292-304.

[22] Benedict SH, Yenice KM, Followill D, Galvin JM, Hinson W, Kavanagh B, et al. Stereotactic body radiation therapy: The report of AAPM Task Group 101. Med Phys. 2010;37(8):4078-101.

[23] Guckenberger M, Andratschke N, Dieckmann K, Hoogeman MS, Hoyer M, Hurkmans C, et al. ESTRO ACROP consensus guideline on implementation and practice of stereotactic body radiotherapy for peripherally located early stage non-small cell lung cancer. Radiotherapy and Oncology. 2017;124(1):11-7.

[24] van Elmpt W, McDermott L, Nijsten S, Wendling M, Lambin P, Mijnheer B. A literature review of electronic portal imaging for radiotherapy dosimetry. Radiotherapy and Oncology. 2008;88(3):289-309.

[25] INTERNATIONAL ATOMIC ENERGY AGENCY. Dosimetry of Small Static Fields Used in External Beam Radiotherapy. Vienna: IAEA; 2017 Nov,.

[26] Das IJ, Ding GX, Ahnesjö A. Small fields: Nonequilibrium radiation dosimetry. Med Phys. 2008;35(1):206-15.

[27] Podgorsak EB, editor. Radiation Oncology Physics. Vienna: INTERNATIONAL ATOMIC ENERGY AGENCY, IAEA; 2005.

[28] Parwaie W, Refahi S, Ardekani MA, Farhood B. Different Dosimeters/Detectors Used in Small-Field Dosimetry: Pros and Cons. Journal of medical signals and sensors. 2018 Jul;8(3):195-203.

[29] Nelms BE, Zhen H, Tomé WA. Per-beam, planar IMRT QA passing rates do not predict clinically relevant patient dose errors. Med Phys. 2011;38(2):1037-44.

[30] Hussein M, Rowshanfarzad P, Ebert MA, Nisbet A, Clark CH. A comparison of the gamma index analysis in various commercial IMRT/VMAT QA systems. Radiotherapy and Oncology. 2013;109(3):370-6.

[31] OmniPro-I'mRT System -user's guide. 2011.

[32] Saminathan S, Manickam R, Chandraraj V, Supe SS. Dosimetric study of 2D ion chamber array matrix for the modern radiotherapy treatment verification. Journal of applied clinical medical physics. 2010;11(2):3076.

[33] Varian Medical Systems. TrueBeam Technical Reference Guide - Volume 2: Imaging. Varian Medical Systems; 2014 Aug.

[34] Varian Medical Systems. Eclipse Photon and Electron Algorithms Reference Guide. Varian Medical Systems; 2017 Oct,.

[35] Ghasemi A, Zahediasl S. Normality tests for statistical analysis: a guide for non-statisticians. International journal of endocrinology and metabolism. 2012;10(2):486-9.

[36] Schlenker E. Tips and Tricks for Successful Application of Statistical Methods to Biological Data. In: Eyster KM, editor. Estrogen Receptors: Methods and Protocols. New York, NY: Springer New York; 2016. p. 271-85.

[37] Williamson DF, Parker RA, Kendrick JS. The box plot: a simple visual method to interpret data. Ann Intern Med. 1989 Jun 1;110(11):916-21.

[38] Middlebrook ND, Sutherland B, Kairn T. Optimization of the dosimetric leaf gap for use in planning VMAT treatments of spine SABR cases. Journal of applied clinical medical physics. 2017;18(4):133-9.

[39] Szpala S, Cao F, Kohli K. On using the dosimetric leaf gap to model the rounded leaf ends in VMAT/RapidArc plans. Journal of Applied Clinical Medical Physics. 2014;15(2):67-84.

[40] Balasingh S, Singh I, Rafic K, Babu S, Ravindran B. Determination of dosimetric leaf gap using amorphous silicon electronic portal imaging device and its influence on intensity modulated radiotherapy dose delivery. J Med Phys(3):129.

[41] Xu Z, Kim J, Han J, Hsia AT, Ryu S. Dose rate response of Digital Megavolt Imager detector for flattening filter-free beams. J Appl Clin Med Phys. 2018;19(4):141-7.

APPENDIX A

An example of a typical stereotactic treatment plan setting for a brain tumor

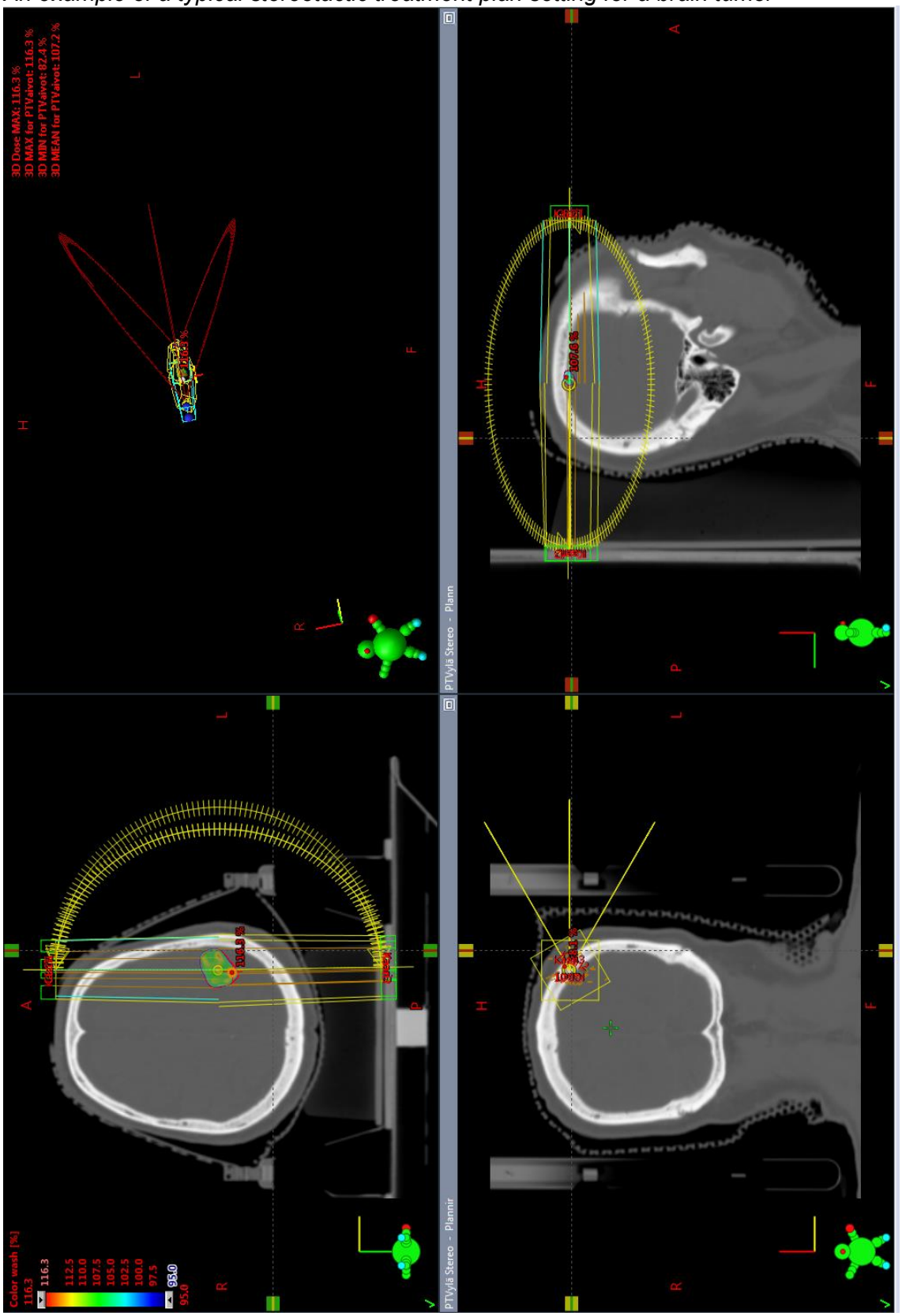

APPENDIX B

An example of a typical stereotactic treatment plan setting for a lung tumor

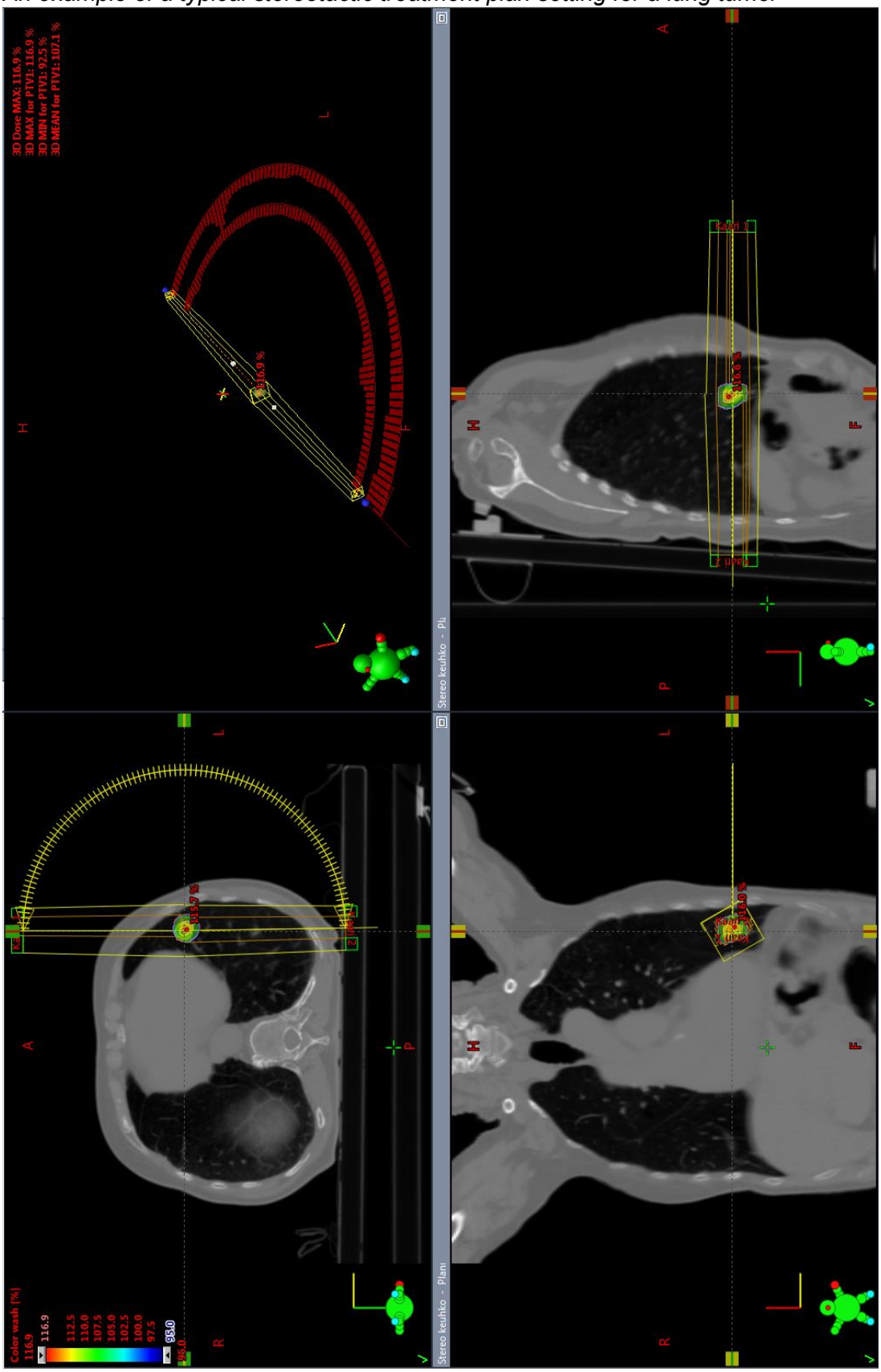

APPENDIX C

An example of a typical stereotactic treatment plan setting for a prostate tumor